Rapid-Scan, Polarimetric Observations of Central Oklahoma Severe Storms on 31 May 2013

ROBIN L. TANAMACHI*

Cooperative Institute for Mesoscale Meteorological Studies, University of Oklahoma, and NOAA/OAR/National Severe Storms Laboratory, Norman, Oklahoma

PAMELA L. HEINSELMAN

NOAA/OAR/National Severe Storms Laboratory, Norman, Oklahoma

(Manuscript received 1 September 2015, in final form 19 October 2015)

ABSTRACT

On 31 May 2013, a polarimetric WSR-88D located in Norman, Oklahoma (KOUN), was used to collect sectorized volumetric observations in a tornadic supercell. Because only a fraction of the full azimuthal volume was observed, rapid volume update times of ~1–2 min were achieved. In addition, the number of pulses used in each radial was larger than is conventional, increasing the statistical robustness of the calculated polarimetric variables. These rapid observations serve as a proxy for those of a future dual-polarized phased-array radar. Through comparison with contemporaneous observations from two nearby dual-polarized WSR-88Ds [Twin Lakes, Oklahoma (KTLX), and near University of Oklahoma Westheimer Airport in Norman (KCRI)], a number of instances in which the rapidly scanned KOUN radar detected or better resolved (in a temporal sense) features of severe convective storms are highlighted. In particular, the polarimetric signatures of merging updrafts, a rapidly descending giant hail core, an anticyclonic tornado, and a dissipating storm cell are examined. These observations provided insights into the rapid evolution of severe convective storms that could not be made (or would have been made with much lower confidence) with current, operational WSR-88D scanning strategies. Possible implications of these rapid updates for the warning decision process are discussed.

1. Introduction

As of 2013, all WSR-88Ds in the U.S. NEXRAD network were upgraded to provide dual-polarized (DP) observations. Information acquired from the polarimetric variables has improved quantitative precipitation estimates, hydrometeor classification algorithms, and discrimination of nonmeteorological echoes such as bioscatterers (e.g., birds and insects), ground clutter, and tornadic debris (e.g., Scharfenberg et al. 2005; Istok et al. 2009). However, the DP WSR-88Ds are still constrained by mechanical scanning to a ~4.5-min volume update time when 14 elevation angles are used, as in volume coverage patterns (VCPs) currently implemented for data collection in convective storms (VCPs 12 and 212; Federal Coordinator for Meteorological Services and Supporting Research 2013).

Forecasters have indicated that faster updates are desirable, particularly at low-elevation angles during rapidly evolving weather situations such as severe convective storms (LaDue et al. 2010). Rapid temporal observations can afford valuable insights into storm evolution by indicating, for example, the changing positions of surface gust fronts (Bluestein et al. 2010), the formation of downbursts and microbursts (Heinselman et al. 2008; Willingham et al. 2011; Kuster et al. 2015b), the intensification of low-level winds (Bluestein et al. 2010; Bowden et al. 2015), the intensification of mid- and low-level rotation that may indicate imminent tornadogenesis (Zrnić et al. 2007; Wurman et al. 2008; Bluestein et al. 2010; Kuster et al. 2012; Wurman et al. 2012; French et al. 2013; Kosiba et al. 2013; Pazmany

* Current affiliation: Department of Earth, Atmospheric, and Planetary Sciences, Purdue University, West Lafayette, Indiana.

Corresponding author address: Robin L. Tanamachi, Dept. of Earth, Atmospheric, and Planetary Sciences, Purdue University, 550 Stadium Mall Dr., West Lafayette, IN 47907.
E-mail: rtanamachi@purdue.edu

DOI: 10.1175/WAF-D-15-0111.1

et al. 2013; French et al. 2014b; Houser et al. 2015; Kurdzo et al. 2015a,b; Kuster et al. 2015a), and increases in reflectivity aloft that may indicate the presence of large hail (Zrnić et al. 2007; Heinselman et al. 2008; Kumjian et al. 2010; Bowden et al. 2015). These insights can increase the lead time for severe weather warnings, allow for the application of updated conceptual models of storm processes, and increase the confidence of operational forecasters in their decisions (Heinselman et al. 2012; Bowden et al. 2015; Heinselman et al. 2015; Kuster et al. 2015a).

To this end, two new dynamic WSR-88D scanning strategies have been introduced recently that reduce the update time for low-level scans. The first is the Automated Volume Scan Evaluation and Termination (AVSET) function (Chrisman 2009), which allows the operational WSR-88D Radar Product Generator (RPG) software to skip one or more of the highest-elevation angles in a VCP. Higher-elevation scans are omitted if they are algorithmically deemed by the RPG to contain unimportant or redundant information. The angle at which the volume terminates depends upon both the aerial coverage and maximum reflectivity of any echoes in the volume. In quiescent weather, the volume may terminate as low as 5.0°. As another example, when scanning a storm (or a group of storms) 100 km or more from the WSR-88D, the uppermost several elevation scans may overshoot the storm tops completely. The RPG can terminate the volume scan early, thereby causing the radar to revisit low-elevation angles more frequently. If there are multiple storms at varying ranges from the radar, the RPG will account for the maximum height of all of the storms in the volume before activating the AVSET scanning. AVSET was incorporated into the operational RPG as of November 2013.

The second dynamic scanning technique is the Supplemental Adaptive Intravolume Low-Level Scan (SAILS) function, which a forecaster can activate to collect one extra 0.5° scan approximately halfway through each volume collection (Chrisman 2014). This technique reduces the revisit time at 0.5°, at the expense of increasing the total update time for the volume. SAILS was incorporated into the WSR-88D RPG software in May 2014. AVSET and SAILS can be used separately or in combination with one another (currently in VCPs 12 and 212 only) to provide up to twice as many 0.5°-elevation scans per data collection period as would be amassed using the original VCP (Chrisman 2014). A new version of SAILS, the Multiple Elevation Scan Option for SAILS (MESO-SAILS), allows for the insertion of up to three intermediate 0.5° scans in a volume (Chrisman 2014), and is currently undergoing testing at selected WSR-88D sites.[1]

Of course, it would be even more desirable to speed up the collection of an entire volume, rather than revisiting only low-elevation angles. Phased-array radar (PAR) offers a promising pathway toward this type of data collection through the use of electronic beam formation and steering (Zrnić et al. 2007; Heinselman and Torres 2011; Priegnitz et al. 2013). PAR technology is considered a strong candidate for the eventual replacement of the WSR-88D (National Research Council 2002). However, owing to significant engineering challenges (Zrnić et al. 2012), only a limited number of PARs currently have DP capability, and most of these have relatively broad azimuthal resolution (Zhang et al. 2011; Orzeł et al. 2011; Bluestein et al. 2014). It is hoped that the eventual successor to the WSR-88D will have both DP and rapid-scanning capability, with data quality and spatial resolution equivalent to or exceeding those of the current WSR-88D network (Brown and Wood 2012).

In the spring of 2013, NSSL conducted the Rapid-Scan Polarization Experiment (RSPE; Burgess et al. 2014), in which a modified DP WSR-88D collected rapid (~1–2 min), sectorized observations in convective thunderstorms over central Oklahoma. The rapid-scanning ability of the DP WSR-88D allowed it to serve as a proxy for a future, operational, DP phased-array radar. A primary goal of this experiment was to observe rapid temporal changes that occur in cyclic supercells. The purpose of this paper is to highlight instances in which rapid, volumetric, DP observations offered unique insights into storm evolution, particularly aspects of those storms that would have not have been resolved or been poorly resolved with current operational WSR-88D scanning strategies. In doing so, we hope to strengthen the case for rapid DP observation capability in the operational radar system that succeeds the WSR-88D.

2. Background

The operational and research benefits conferred by rapidly updated reflectivity Z and Doppler velocity V_r observations are already well documented (e.g., Heinselman et al. 2008; LaDue et al. 2010; Heinselman et al. 2015; Tanamachi et al. 2015). Therefore, in this study, we focus exclusively on DP observations related to severe weather (large hail and tornadoes). We refer the reader to the comprehensive review of DP

[1] Information is available online (http://www.nws.noaa.gov/os/notification/tin15-04wsr-88d_mesosails.txt).

signatures in storms by Kumjian (2013), and only briefly summarize a few of those signatures here. Unless otherwise noted, these features have been observed at S, C, and X bands.

a. Differential reflectivity columns

Columnar extensions of relatively enhanced differential reflectivity Z_{DR} above the freezing (0°C) level are now generally accepted as a signature of oblate drops of supercooled water lofted by an active updraft (Illingworth et al. 1987; Loney et al. 2002; Kumjian and Ryzhkov 2008; Romine et al. 2008; Snyder et al. 2013; Kumjian et al. 2014). The Z_{DR} column shows significant promise for use in the automated detection of updrafts in convective storms (Snyder et al. 2015). In supercells, this feature (or a series of them) is generally located at midlevels (4–6 km AGL) near the hook echo.

b. Tornado debris signature

When observed in association with other features supporting the likelihood of a tornado (e.g., a supercell hook echo with strong azimuthal shear), the tornado debris signature (TDS) is a circular or semicircular region at low levels characterized by a relatively low (<0.9) copolar cross-correlation coefficient ρ_{hv} and Z_{DR} near or slightly less than zero. These measurements indicate the presence of randomly oriented, nonmeteorological scatterers (i.e., lofted tornado debris) (Ryzhkov et al. 2005b; Bluestein et al. 2007; Kumjian and Ryzhkov 2008; Palmer et al. 2011; Schultz et al. 2012; Tanamachi et al. 2012; Bodine et al. 2014; Wurman et al. 2014). It is particularly useful for tornado detection when the tornado occurs in a low-visibility situation, such as at night, or when it is obscured from view by intervening precipitation.

c. Z_{DR} arc

The Z_{DR} arc is a curved, low-level (<2 km AGL) area of enhanced Z_{DR} (e.g., >3 dB) along the inflow edge of the forward-flank precipitation shield (Kumjian and Ryzhkov 2008). It indicates the presence of a drop size distribution biased toward larger (and hence more oblate) raindrops. Based on the results of empirical observations (Romine et al. 2008; Van Den Broeke et al. 2008; Friedrich et al. 2013) and numerical simulations (Kumjian and Ryzhkov 2009; Jung et al. 2010; Kumjian and Ryzhkov 2012; Dawson et al. 2014, 2015), the Z_{DR} arc is now generally believed to form as a result of hydrometeor size sorting in the presence of strong storm-relative low-level inflow beneath the supercell. Intensification of the Z_{DR} arc along the inflow edge of the forward flank is hypothesized to be indicative of increased inflow into the supercell, a possible precursor to strengthening and/or tornadogenesis (Crowe et al. 2012) or mesocyclone cycling (Crowe et al. 2010; Kumjian et al. 2010; French et al. 2014a; Kuster et al. 2015a).

d. Large hail signatures

In supercells, large hail is anticipated near the overlap of the precipitation core and updraft, which can support extended lofting of (and hence accumulation of water by) large hailstones above the freezing level. Operational meteorologists can infer the presence of large hail by interrogating DP observations of supercells for enhanced Z, near-zero Z_{DR} (from tumbling hailstones) (Bringi et al. 1984; Aydin et al. 1986), and optionally, low specific differential phase K_{DP} (Heinselman and Ryzhkov 2006; Van Den Broeke et al. 2008). Large, dry hail above the freezing level can also generate a relative minimum in ρ_{hv} because the accumulation of supercooled drops by the hailstone can cause protuberance formation, resulting in nonspherical hail shapes (Balakrishnan and Zrnic 1990). This large hail signature can be particularly prominent if it occurs within an area of enhanced Z_{DR}, such as a Z_{DR} arc. The large hail signature is likely to be more difficult to detect at X band, because substantial attenuation can cause complete X-band signal extinction before the radar pulses reach the storm core.

3. Data and methodology

We focus in this study on observations collected by the Norman, Oklahoma, DP WSR-88D (KOUN; Fig. 1). KOUN was one of the principal instruments used to demonstrate the operational advantages of polarimetric observations during the Joint Polarization Experiment (JPOLE; Ryzhkov et al. 2005a; Scharfenberg et al. 2005). Results of this research were key motivators for the nationwide DP upgrade to the NEXRAD network.

In spring 2013, NSSL engineers modified the antenna control system software of KOUN to allow for on-demand, customized, sectorized scanning as part of the RSPE. Although still mechanically constrained to scan one elevation angle at a time, these modifications enabled ~1–2-min volume update time, emulating the rapid scanning of the National Weather Radar Testbed (NWRT) PAR (Zrnić et al. 2007). Data collected in this way were processed in "superresolution" mode (0.5° azimuthal resolution, 250-m radial resolution) rather than "legacy" mode (1.0° azimuthal resolution, 250-m radial resolution) at all elevation angles. In superresolution mode, half the conventional number of pulses is used to calculate moments in each gate (Brown et al. 2002, 2005a; Kumjian et al. 2010). The end result is finer

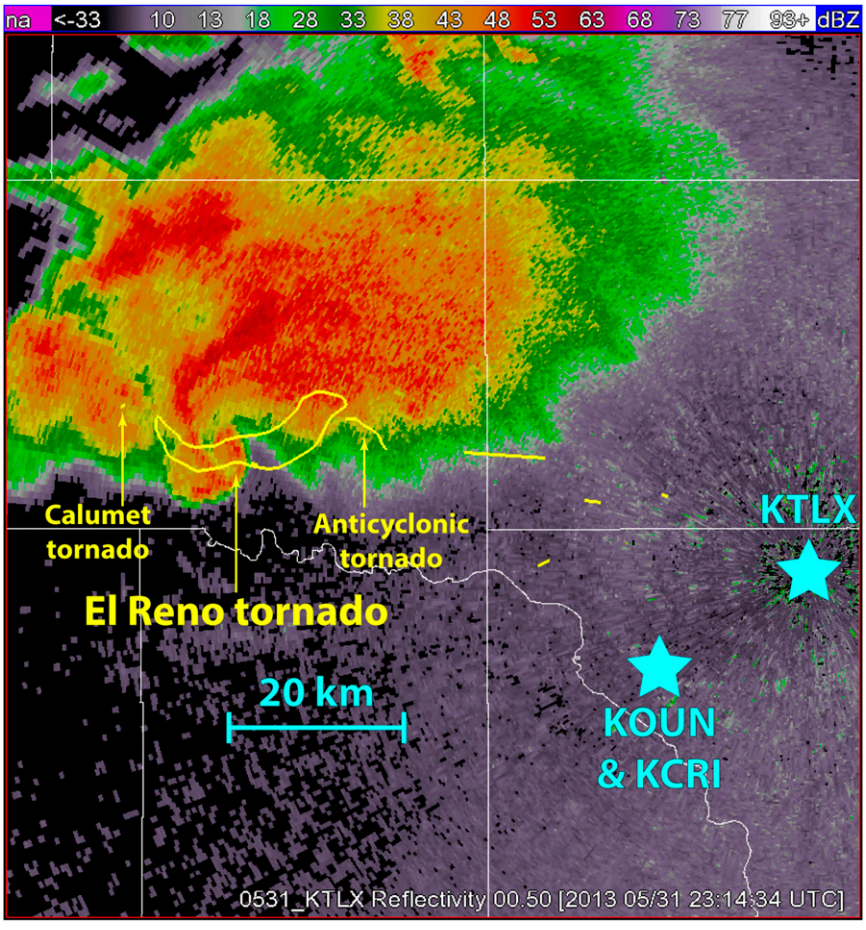

FIG. 1. KTLX observations of reflectivity (dBZ) at 2314 UTC at an elevation angle of 0.5°, showing the El Reno supercell while the El Reno tornado was about halfway through its track (closed yellow contour). Additional tornado tracks from 31 May are shown by yellow line segments. The locations of KTLX, KOUN, and KCRI are annotated by cyan stars. (The track of the anticyclonic tornado is courtesy of J. Snyder.)

spatial resolution in the azimuth, at the expense of statistical robustness of moments calculated at each gate. Superresolution processing, using 32 pulses per radial at elevation angles at or below 1.5°, is standard for most WSR-88D products at the time of this writing. The scanning strategy used and the superresolution processing applied to the KOUN observations collected in 2013 (which had 128 pulses per radial) are similar to those used by Kumjian et al. (2010), except that the VCP was completely customizable. During data collection, the radar operator supplied the width of the sector and a set of elevation angles via the command line. Such a scanning strategy could not be used operationally in the current WSR-88D network, for obvious reasons. Rather than revisiting every beam position uniformly as in the operational VCPs, this practice served as a rough proxy for automated (or semiautomated) PAR observing strategies in which beam positions intersecting storms are revisited more frequently than those outside the storms (Priegnitz et al. 2013).

On 31 May 2013, KOUN collected rapid, sectorized observations (with the sector reoriented from westward pointing to northward pointing as the storms progressed from west to east, north of KOUN's longitude) from 2145 to 0412 UTC (Melnikov et al. 2014). The VCP used was relatively shallow (elevation angles: 0.5°, 1.0°, 1.5°, 2.0°, 3.0°, 4.0°, 5.0°, 6.0°, 8.0°, and 10.0°) compared to the operational VCP 12. The KOUN observations were not available to forecasters in real time. However, Kuster et al. (2015a) explored the hypothetical impacts of rapidly updated reflectivity and velocity observations collected by PAR on the operational warning decision process for 31 May 2013. It was conjectured that the rapid updates could have enabled forecasters to detect rapid intensification of tornado-related features (e.g., the low-level mesocyclone) a few minutes earlier than

with conventional updates, to forecast the movement of those features more accurately, and to more effectively apply updated conceptual models of mesocyclone cycling and tornadogenesis processes.

In the present study, we provide side-by-side comparison of KOUN observations on 31 May 2013 with those collected by two nearby WSR-88Ds. The first is the operational WSR-88D at Twin Lakes, Oklahoma (KTLX; Fig. 1), which operated in VCP 12 (with 14 elevation angles spanning 0.5°–19.5°). Although KTLX had AVSET enabled in 2013, storms occurred within 100 km of the radar throughout the study period, so the volumes were never truncated early, and the KTLX volume update time was 4.1 min. The second radar is the National Weather Service (NWS) Radar Operation Center's WSR-88D (KCRI; Fig. 1), located <1 km from KOUN (near University of Oklahoma Westheimer Airport in Norman), which is used for development and testing. KCRI operated in SAILS mode within VCP 12 on 31 May 2013, revisiting the 0.5°-elevation angle roughly halfway through each 5.1-min volume scan. Therefore, KCRI collected a 0.5°-elevation scan every 2–3 min.

After initial processing, we inspected the KOUN, KTLX, and KCRI observations using the Warning Decision Support System–Integrated Information (WDSS-II; Lakshmanan et al. 2007) graphical user interface. We also applied the WDSS-II azimuthal shear detection algorithm (Smith and Elmore 2004) to the three sets of Doppler velocity observations in order to highlight areas of rotation.

4. DP signatures in the 31 May 2013 El Reno, Oklahoma, storm

The central Oklahoma spring severe weather season in 2013 was quite active. Tornadic storms on 19, 20, and 31 May 2013, which resulted in the loss of dozens of lives, captured national attention (National Weather Service 2014a). We focus on a high-precipitation supercell that produced multiple tornadoes and large hail west of the Oklahoma City metropolitan area (hereafter the El Reno storm; Fig. 1) on 31 May 2013 (National Weather Service 2014b; Witt 2014; Bluestein et al. 2015; Kuster et al. 2015a). This storm is notorious within the severe weather research community for producing an exceptionally wide, multiple-vortex tornado near El Reno (hereafter the El Reno tornado; track shown in Fig. 1) that killed four storm chasers, the first known tornado-attributable fatalities in the history of the practice (Snyder and Bluestein 2014; Wurman et al. 2014). Four additional fatalities also resulted from the El Reno tornado, which lasted from 2303 to 2343 UTC (National Climatic Data Center 2014). At least 10 additional, smaller tornadoes were documented in this storm cluster (National Weather Service 2014b).

Bluestein et al. (2015) present the synoptic- and mesoscale weather conditions preceding the El Reno storm. Detailed accounts of the warning process on this date can be found in National Weather Service online documentation (National Weather Service 2014b) and a subsequent NWS Service Assessment (National Weather Service 2014a). Tornadoes were rated on the enhanced Fujita (EF) scale (McDonald and Mehta 2006).

a. *Merging updrafts*

We infer the presence of midlevel updrafts (MLUs) in severe convective storms from Z_{DR} columns. These MLUs were evident in CAPPI plots of Z_{DR} as local maxima above the freezing level (e.g., Illingworth et al. 1987; Kumjian et al. 2014), which was 4.1 km MSL or 3.8 km AGL (Fig. 2). KOUN collected 10 volumes between 2237 and 2253 UTC (Figs. 3a–j); while KTLX collected 4 (Figs. 3k–n) and KCRI only 3 (Figs. 3o–q). [KCRI Z_{DR} observations at 2253:09 UTC (Fig. 3r), although occurring outside the 2237–2253 UTC window, are included in order to show morphological consistency with observations by KOUN at 2252:54 UTC (Fig. 3j).] The KOUN rapid volume update time, and in particular, the relatively frequent midlevel scans, allow Z_{DR} columns (and hence inferred updrafts) to be more easily detected and tracked. It can be seen in the CAPPI displays of Z_{DR} at 5 km AGL (Fig. 3) that the El Reno storm possessed a single, primary MLU (labeled 1; hereafter MLU1), and that numerous other updrafts (MLU2–MLU6) merged into it from 2237 to 2252 UTC. These updrafts originated from two primary sources (with respect to storm motion, which was toward the east): the right flank of the storm (MLU2, MLU3, and MLU6) and the rear flank of the storm (MLU4 and MLU5). The relative temporal coarseness of the midlevel KTLX and KCRI observations obfuscates several of these MLU mergers. In particular, MLU3, which lasted about 8 min before its merger with MLU1, is detected in six KOUN volumes (Fig. 3a–f) but in only one volume by KTLX (Fig. 3l) and two volumes by KCRI (Figs. 3o,p). In the KTLX and KCRI observations (Figs. 3k–r), one of the short-lived updrafts (MLU6) and its merger into MLU1, which were detected in two KOUN volumes (Figs. 3g,h), were missed entirely.

Because Z_{DR} columns are located at midlevels and may only last a few minutes, frequent scans are required at middle VCP tilts to track them. Additionally, the accurate assessment of the depth of the Z_{DR} column, which can indicate the strength of the updraft (Kumjian

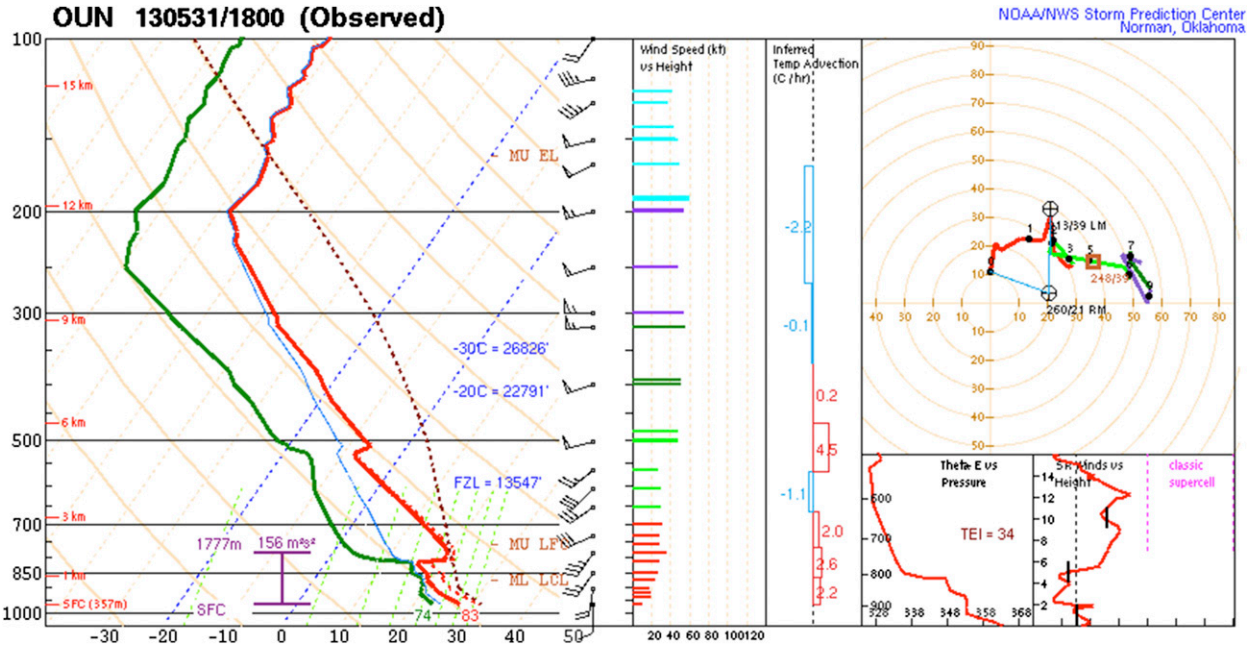

FIG. 2. (left) Skew T–log$p$ thermodynamic chart and (right) accompanying hodograph for the rawinsonde observations from Norman at 1800 UTC 31 May 2013, showing that the freezing level (denoted FZL) is 4.1 km MSL or 3.8 km AGL. (Source is the NWS Storm Prediction Center; a detailed explanation of the calculated parameters can be found online at http://www.spc.noaa.gov/exper/soundings/help/index.html.)

2013), requires dense vertical sampling at midlevels (Snyder et al. 2015). For example, if the column is 50 km (150 km) from the radar and extends from 4 to 7 km AGL, a WSR-88D operating in VCP 12 will sample it with four (three) tilts ranging from 4.0° to 8.0° (from 1.3° to 2.4°). This relatively coarse vertical sampling at midlevels is a consequence of denser vertical sampling at low levels, which is needed to more readily detect mesocyclone intensification (Brown et al. 2005b) and possibly a TDS. While this additional observation at low levels is of crucial importance to forecasters, it is collected at the expense of observations aloft. More rapid scanning would enable denser sampling at midlevels without penalizing low-level update time.

It has been shown in previous studies that merging storms and attendant updraft interactions (Wurman et al. 2007; Hastings et al. 2012; Tanamachi et al. 2015) may have an impact on tornado production potential. Whether these particular updraft mergers on 31 May 2013 were consequential for tornadogenesis is beyond the scope of this study. In a previous study, it was found that a storm merger was associated with temporary weakening of the primary updraft in a tornadic storm that, coincidentally, also occurred near El Reno on 24 May 2011 (Tanamachi et al. 2015). In the 2011 El Reno storm, the disruption in the primary storm's updraft and tornado production was attributed to midlevel mesocyclone cycling. A "bridging" updraft developed between the El Reno storm and the merging storm as a result of an outflow boundary collision occurring at the surface. In contrast, the 2013 El Reno storm's MLU1 showed a pronounced increase in aerial coverage following its merger with MLU3 at 2246 UTC (Fig. 3g), with the Z_{DR} column expanding into a Z_{DR} ring (Kumjian and Ryzhkov 2008). Tornado production commenced at 2255 UTC with the formation of the Calumet, Oklahoma, tornado (Fig. 1) (Wurman et al. 2014; Bluestein et al. 2015; Kuster et al. 2015a), and extremely large hail (discussed in the next section) was documented east of MLU1 at 2305 UTC. We speculate that because the merging storms were immature compared to those studied by Tanamachi et al. (2015), they did not have deep, expansive cold pools and, therefore, did not generate outflow boundary collisions and bridging updrafts that disrupted the primary storm's midlevel updraft on 24 May 2011.

Using a greater number of pulses to calculate the KOUN moments (128 vs 32 for KTLX and KCRI) greatly reduces the variance in the moments calculated (Doviak and Zrnić 1993). In particular, we expect the standard deviation of Z_{DR} to be reduced from about 0.3 dB to less than 0.2 dB (their Fig. 6.11). The effects of this practice on data quality are especially evident when comparing KOUN observations of Z_{DR} to those from

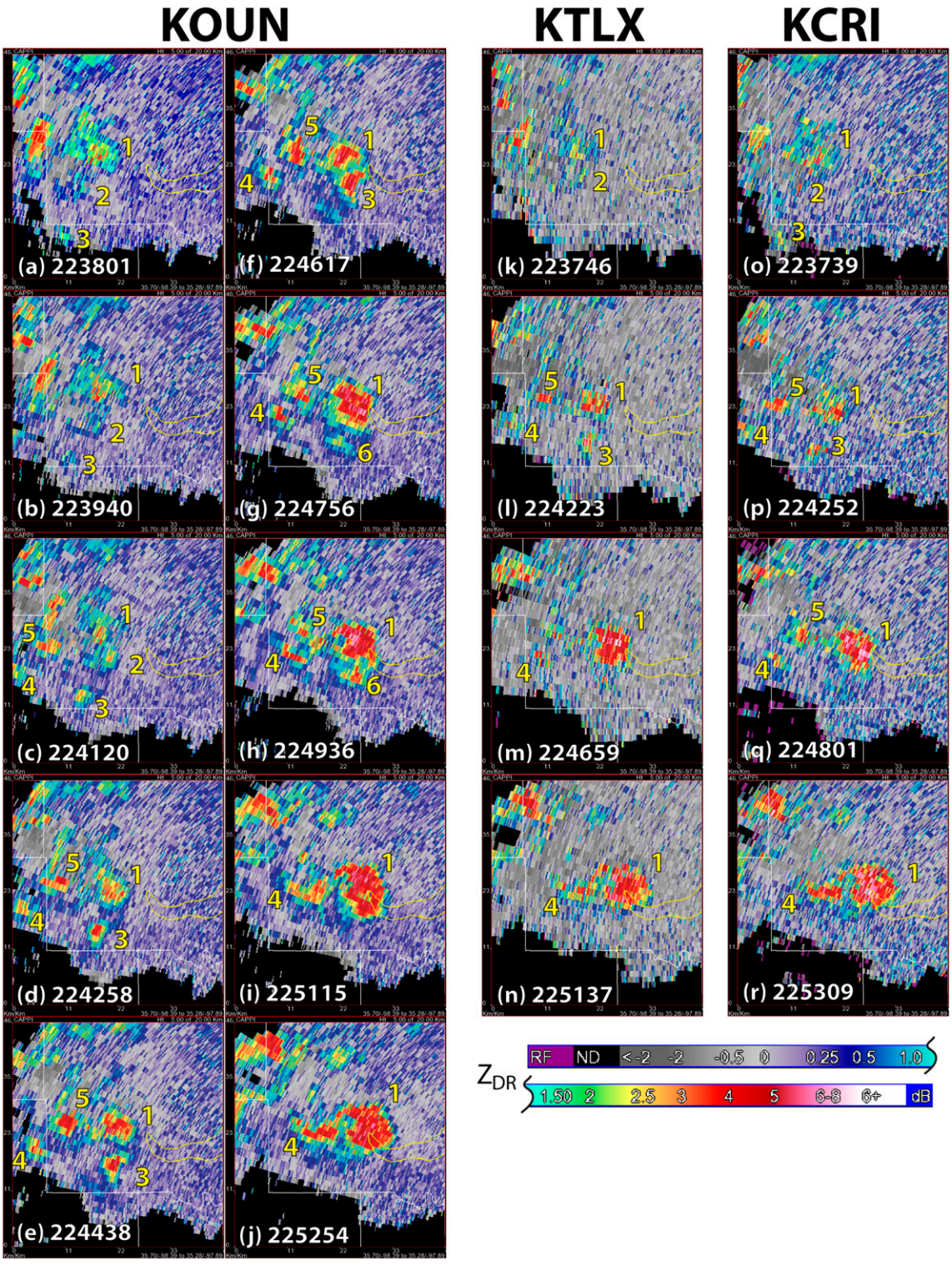

FIG. 3. CAPPI plots of Z_{DR} (dB) at 5 km AGL in the El Reno storm, as seen by (a)–(j) KOUN, (k)–(n) KTLX, and (o)–(r) KCRI. The times shown in each panel (UTC) are those at which the lowest elevation sweep (0.5°) was collected in the volume used to generate the CAPPI. County boundaries are drawn in thin white lines; yellow contours are tornado tracks. MLUs are numbered in yellow.

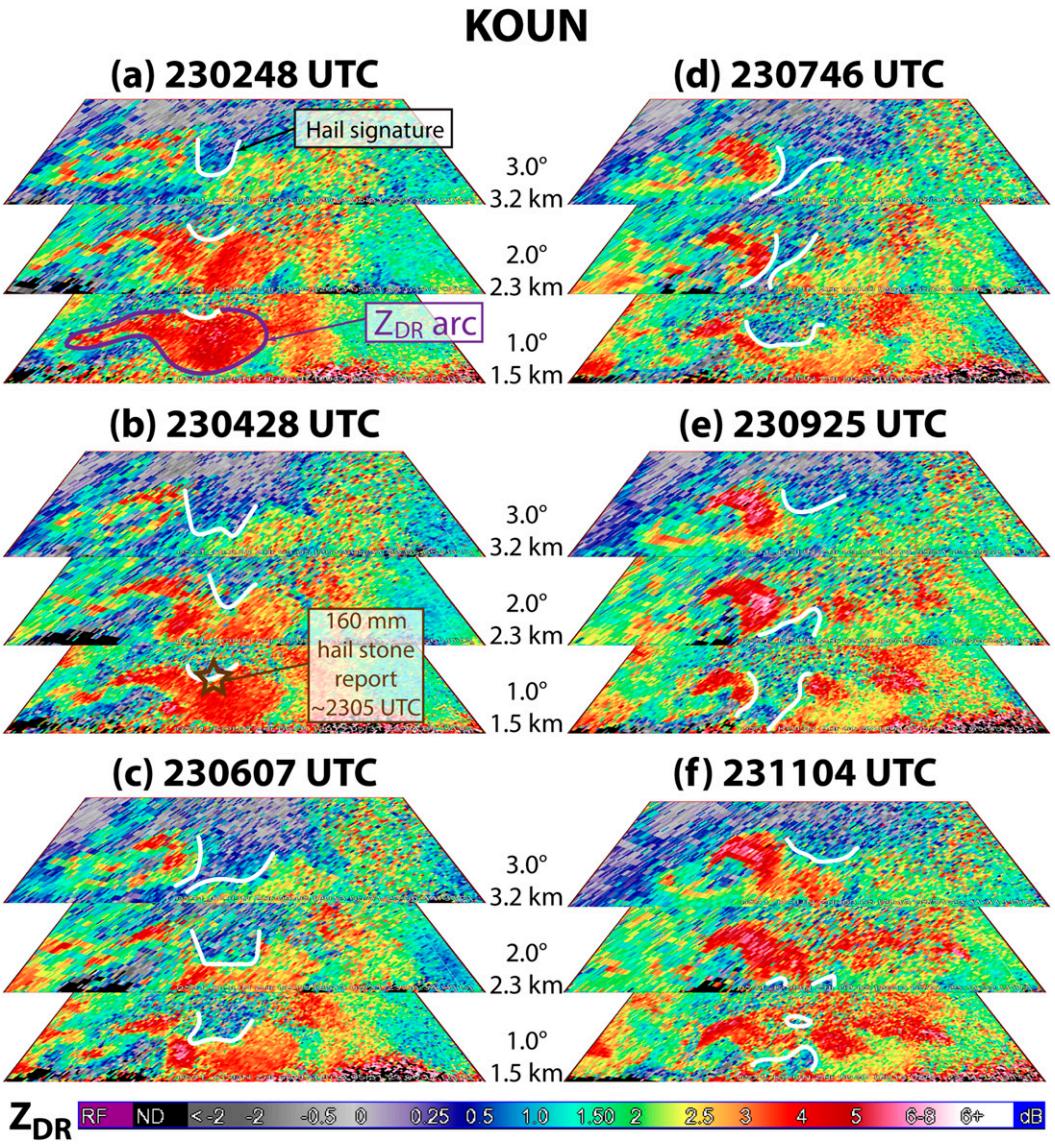

FIG. 4. KOUN observations of Z_{DR} (dB) in a descending hail core from 2302 to 2312 UTC. The times shown in each panel (UTC) are those at which the volume collection began (i.e., the 0.5°-elevation scan started). The heights shown are the beam heights at the center of the domain. The purple outline in (a) (omitted in subsequent panels for clarity) denotes the Z_{DR} arc, the heavy white outline denotes the hail signature, and the brown star is centered on the approximate location and time of the 160-mm hailstone (Witt 2014).

KTLX and KCRI (e.g., Fig. 3). The relative noisiness of the KTLX and KCRI observations of Z_{DR} obscured some of the smaller, less intense Z_{DR} columns. For example, it was only upon retroactive inspection of near-contemporaneous KOUN observations (Fig. 3a) that MLU2 could be discerned in the KTLX and KCRI observations (Figs. 3k,o).

b. *Descending hail signature*

In addition to tornadoes and copious rainfall, the El Reno storm also produced giant hail (National Weather Service 2014a,b). One hailstone measuring 160 mm in diameter, the fifth largest documented in the United States to date, fell south of El Reno at approximately 2305 UTC (Witt 2014).

KOUN observed a distinct DP signature indicative of this giant hail between 2302 and 2312 UTC (Fig. 4). This signature consisted of a descending volume wherein the Z_{DR} was near zero. We are confident that this feature represented large hail because it was also associated with relatively high Z (not shown) and depressed ρ_{hv} (~0.8; not shown), and, most importantly,

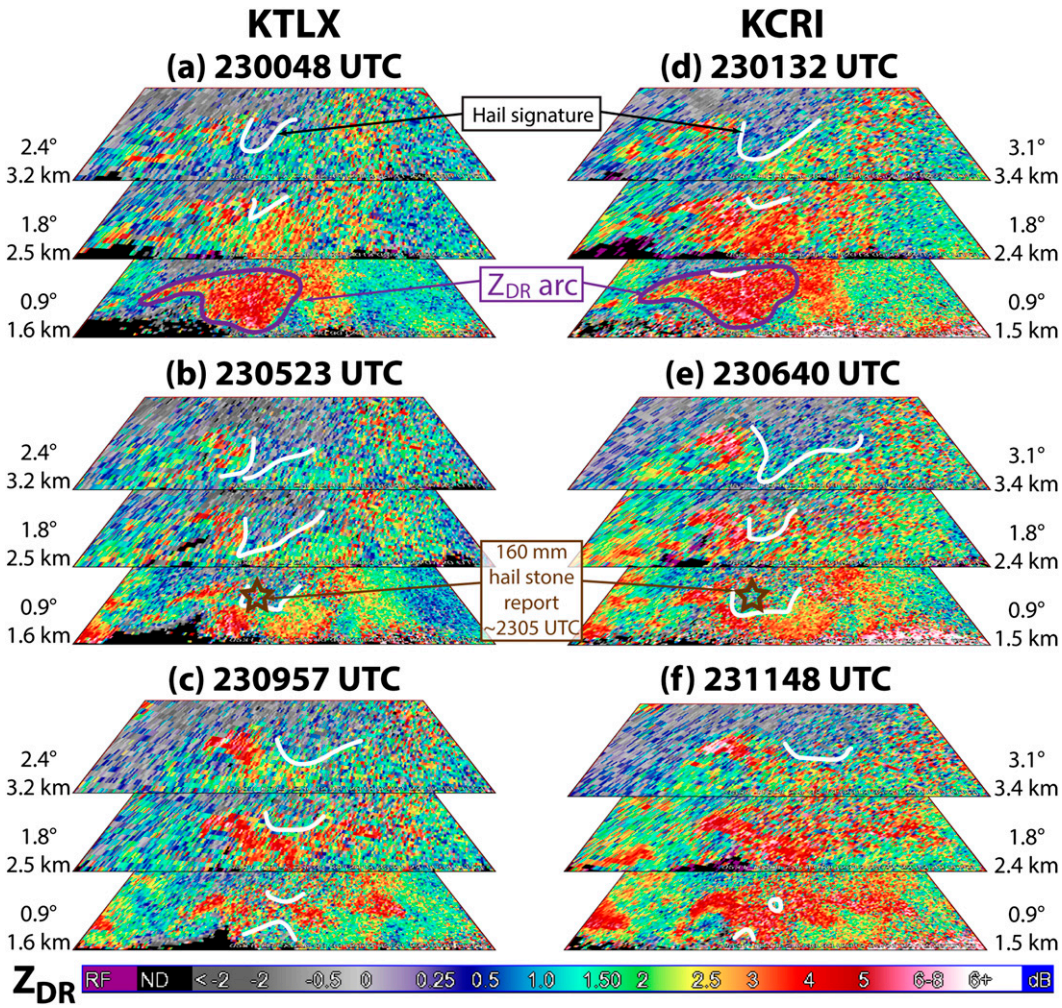

FIG. 5. As in Fig. 4, but for (a)–(c) KTLX and (d)–(f) KCRI observations from 2300 to 2312 UTC.

because large, tumbling hailstones with many protuberances were documented near the time and location of the signature (Witt 2014). We characterize this particular low-level hail signature as a transient disruption in the Z_{DR} arc. Similar polarimetric signatures attributed to large hail descending through the Z_{DR} arc (or other areas of enhanced Z_{DR}) have been reported elsewhere in the literature (Kumjian et al. 2010; Picca and Ryzhkov 2012; Dawson et al. 2014; Kuster et al. 2015b). Other, similar hail descent signatures (not shown) were observed before and after this one. The hail signature was evident because of its contrast to the enhanced Z_{DR} in the Z_{DR} arc. Were the enhanced area of Z_{DR} not present, this signature would have been more difficult to discern.

KOUN captured the descent of this feature over six volume scans (Fig. 4). In contrast, KTLX and KCRI only captured this signature in three volume scans each (Fig. 5). KOUN and KCRI both captured the initial "bite" out of the northern edge of the Z_{DR} arc at 2302 UTC (Figs. 4a and 5d). However, the closest (in time) KTLX volume (Fig. 5a) does not show this early incursion of the hail signature into the Z_{DR} arc, because it was collected about a minute too early (2300:47 UTC). In the KOUN observations (Fig. 4), it is clear that the hail signature passes through the Z_{DR} arc from north to south. The south- and downward progress of this feature with height is captured reasonably well by KCRI and KTLX (Fig. 5), but the feature's exit from the southern edge of the Z_{DR} arc at 2311 UTC is not well captured by either. In addition, this hail signature was difficult to discern in the noisier KCRI and KTLX Z_{DR} fields (Fig. 5), which were calculated using one-quarter the number of pulses KOUN used (32 vs 128). As was the case with Z_{DR} columns in this storm (section 4a), the hail signature sometimes had to be identified in KTLX and KCRI observations based on the closest (in time and space) KOUN observations.

This Z_{DR} arc disruption would probably have limited utility within the context of severe thunderstorm warning issuance, because a supercell mature enough to possess a distinct Z_{DR} arc would probably already have a severe thunderstorm warning in effect (V. Mahale and T. Lindley 2015, personal communication). However, we suggest that the feature might have other applications within the context of the severe thunderstorm warning process. For example, the hail signature could be mentioned in severe weather statements or other follow-up products issued after the initial warning, or used for verification of hail in areas of sparse spotter reports.

c. *Anticyclonic tornado*

During the El Reno tornado, forecasters were keenly aware of the threat of additional tornadoes nearby, since large, violent tornadoes seldom occur alone (Agee et al. 1976; Edwards 2014). In the 0.5°-elevation scans from all three WSR-88Ds, dozens of low-level azimuthal shear extrema with magnitudes exceeding 0.01 s^{-1}, some anticyclonic, formed and weakened near the El Reno tornado (e.g., Figs. 6a, 7a, and 8a). It was not immediately obvious which of these maxima might be associated with additional tornadoes. About halfway through the El Reno tornado's life cycle, at 2329 UTC, an anticyclonic tornado developed 4 km southeast of the El Reno tornado (Wurman et al. 2014; Bluestein et al. 2015), in a zone of anticyclonic azimuthal shear (AS; Fig. 6b). It generated a curving, 6.5-km damage track (Figs. 1 and 6) as it tracked southeastward toward Mustang, Oklahoma, then dissipated at 2341 UTC (National Weather Service 2014b). Bluestein et al. (2015) found good agreement between this surface damage track (later rated EF2) and low-level observations of this tornado made by a rapidly scanned, mobile, DP, X-band Doppler radar from 2332 to 2341 UTC. The developing anticyclonic tornado was already contained within a tornado warning polygon issued at 2328 UTC for the much larger El Reno tornado, so no additional tornado warning was issued (Bluestein et al. 2015; R. Smith 2015, personal communication).

The timing of the anticyclonic tornado's formation (2329 UTC) could hardly have been worse for detection by KTLX, as it formed just after a prior 0.5° scan at 2328:40 UTC (Fig. 7a). Indications of the anticyclonic tornado appeared in the KOUN observations 1–3 min before those from KCRI and KTLX. The AS maximum corresponding to the developing anticyclonic tornado first exceeded 0.01 s^{-1} in the KOUN, KTLX, and KCRI observations at 2329:13, 2333:16, and 2330:19 UTC, respectively, with TDSs (Ryzhkov et al. 2005b) first detected at 2330:52, 2333:16, and 2330:19 UTC, respectively (Figs. 6–8). Significantly, what appears to be a pre-TDS appeared briefly at 2327:34 UTC in the KOUN observations (Figs. 6k,u), weakened at 2329:13 UTC (Figs. 6l,v), then reappeared at 2330:52 UTC (Figs. 6m,w). We speculate that this pre-TDS, which was not associated with surface damage, may indicate an interrupted attempt at tornadogenesis (e.g., the surface vortex could have weakened around 2328 UTC, then reintensified at 2329 UTC). It is also possible that the pre-TDS represents a local concentration of lofted dust or debris produced by either the main El Reno tornado or its associated rear-flank downdraft (RFD). However, its persistent association with a local maximum in AS (Fig. 6a) makes this possibility less likely. Additional, rapid, low-elevation polarimetric observations would be necessary to confirm this speculation; however, Bluestein et al. (2015) were not collecting observations at this time because they were evacuating the projected path of the El Reno tornado, and the anticyclonic tornado [which is said to have formed at "~2328 UTC"; Wurman et al. (2014)] was not the focus of the study by Wurman et al. (2014).

KOUN collected nine 0.5° scans between 2328 and 2342 UTC (Figs. 6b–j, 6l–t, and 6v–dd), as many as KTLX and KCRI put together (Figs. 7a–c, 7e–g, and 7i–k, as well as Fig. 8). KCRI, operating in SAILS mode, only collected one more 0.5° scan than KTLX (five vs four) during this 14-min period because of its longer-duration VCP (Figs. 7 and 8).

The TDSs observed by all three WSR-88Ds closely followed the track presented by Bluestein et al. (2015) (Fig. 9), which may be incomplete owing to a lack of mobile radar data coverage in the 4 min after the tornado formed (at 2329 UTC). However, KOUN collected seven 0.5° scans of the TDSs during the tornado's 12-min life span (Figs. 6c–i, 6w–cc, as well as Fig. 9a), while, owing to VCP timing, KTLX collected only two (Figs. 7f,g,j,k and 9b) and KCRI five (Figs. 8f–o and 9c). More detail of the tornado's motion and translational speed can be inferred from more frequent DP observations. In particular, the KOUN TDS track (Fig. 9a) and, to a lesser extent, the KCRI TDS track (Fig. 9c) show that the tornado accelerated away from its parent storm upon turning toward the southeast at 2334 UTC, then slowed at 2337 UTC, before finally dissipating. The KTLX TDS track (Fig. 9b) does not exhibit these details owing to the temporal coarseness of the observations.

We have shown an example in which the temporal coarseness of the operational WSR-88D scans delayed detection of a TDS by 3–4 min. Supplemental observations are required to ameliorate this issue. In addition, mobile radar observations (e.g., Wurman et al. 2014; Bluestein et al. 2015) and observations by current

''gap filling'' low-level radars (e.g., Maki et al. 2008; McLaughlin et al. 2009) are not collected consistently in tornadic storms and are generally not available to forecasters in real time. Rapid-scan DP updates from operational radars would likely increase forecaster confidence in the tornado's presence, persistence, and direction of movement. These insights could potentially have a positive influence on forecaster decisions about the location, size, and duration of issued tornado warning polygons.

d. Dissipating convective cell

While inspecting the KOUN observations from the pretornadic period, our attention was drawn to a nearly circular region of anomalously low Z_{DR} (~0.25 dB) near the surface, extending southward from the intensifying El Reno storm (Fig. 10a). This low-level, low-Z_{DR} appendage was associated with relatively low reflectivity (<20 dBZ; Fig. 10b) and relatively high ρ_{hv} (~0.96–1.0; Fig. 10c), leading us to infer that it was composed primarily of small raindrops.

Looking backward in time, we found that this low-Z_{DR} feature had previously been a high-Z_{DR} (~5 dB) feature (Figs. 11a–m); its origins lay in a Z_{DR} arc–like region of a weak storm cell (Fig. 11n) whose updraft collapsed before the cell merged into the El Reno storm. This smaller storm initiated a few kilometers east of the dryline around 2200 UTC (as seen in KTLX observations, not shown, and satellite imagery; Fig. 11a) and, although it did not exhibit any appreciable low- (Fig. 12d) or midlevel rotation (not shown), it possessed (in Z) the ''flying eagle'' shape and a small downsheared precipitation shield characteristic of a developing supercell (Figs. 11n and 12c; Kumjian and Schenkman 2008). Despite forming in a relatively uncontaminated, sunny environment (likely similar to that shown in Fig. 2) at the southern end of the El Reno storm complex (Fig. 12a), the updraft of this smaller storm was not sustained, possibly as a result of subsequent anvil shading (Fig. 12b; Frame and Markowski 2013) and/or mesoscale subsidence. Low-level reflectivity in this storm's precipitation core never exceeded 30 dBZ (Figs. 11n–z and 12c), and Doppler velocities near its base were clearly divergent (Fig. 12d), suggesting the core was dominated by a strong downdraft.

The last MLU pulse in this cell (inferred from KOUN Z_{DR} observations at 3.0°, or 6 km AGL at the cell's range of 94 km; Figs. 12e–g) occurred along its western edge at about 2219 UTC (Fig. 12e). The corresponding Z_{DR} column peaked in intensity at 2222 UTC (Fig. 12f), then weakened and collapsed over the next 13 min (e.g., Fig. 12g), possibly because anvil shading (Fig. 11b) decreased the surface temperature below that required for autoconvection (35.6°C; Fig. 2), or because subsidence outside the intensifying El Reno storm cluster reinforced the capping inversion there (Fig. 2). Without the sustained updraft, the raindrop source region in the small cell was effectively shut off, and no more raindrops entered its precipitation shaft from aloft. We hypothesize that size sorting resulting from air drag and south-southwesterly near-surface flow (Kumjian and Ryzhkov 2012; Dawson et al. 2014) led to large drops reaching the surface first on the storm's southwest flank, creating the Z_{DR} arc–like feature (Fig. 11a). We further hypothesize that once the large drop supply was exhausted, medium-sized drops reached the surface, followed by the smallest drops. This sequential fallout of sorted drops would have resulted in the observed steady decrease in Z_{DR} in the western flank of the dying storm's precipitation shield at all levels up to 5 km AGL (although only the lowest tilt is shown in Figs. 11a–m), forming the low-Z_{DR} appendage (Fig. 10a), and ended with the absorption of the low-Z_{DR} appendage into the eastern flank of the El Reno storm (Fig. 11m).

KCRI and KTLX observations of the dissipating storm were both temporally coarser (owing to their respective full-disk VCPs) and noisier (owing, once again, to the smaller number of pulses used). KTLX sampled the low-level, low-Z_{DR} appendage roughly half as often (about every 4.5 min; e.g., Figs. 13a,b) as did KOUN. Notably, KTLX missed the intermediate stages of the appendage's transition from a relatively high-Z_{DR} feature to a relatively low-Z_{DR} feature (Figs. 11d–g) during the 4.5-min gap between 0.5° scans at 2223:55 and 2228:32 UTC (Figs. 13a,b). This gap could lead an observer to misinterpret the Z_{DR} arc–like feature in the dissipating storm as having moved north, rather than transitioning to a low-Z_{DR} feature. KCRI, operating in SAILS mode, collected eight 0.5° scans between 2218 and 2238 UTC (not shown), capturing much the same evolution of the low-level, low-Z_{DR} appendage as did KOUN at 0.5°. However, KOUN collected a dozen 0.5° scans during this same 20-min interval (Figs. 11a–l), owing to KCRI's longer SAILS volume update time. Similar to previously discussed merging updrafts (section 4a), the final MLU pulse associated with the dissipating storm was sampled much less frequently by both KTLX (not shown) and KCRI (Figs. 13c–e) than it was by KOUN. Between 2219 and 2235 UTC, KTLX, KCRI, and KOUN collected three, three, and seven scans in this MLU, respectively. With the coarser time resolution of the KTLX and KCRI observations, it was not as clear that the updraft pulse was continuous in time. Owing to the relative noisiness of the KTLX and KCRI Z_{DR} observations, in some scans (e.g., Fig. 13c) it was not even clear whether a Z_{DR} column was present; it had to be inferred from looking at the KOUN Z_{DR} observations first.

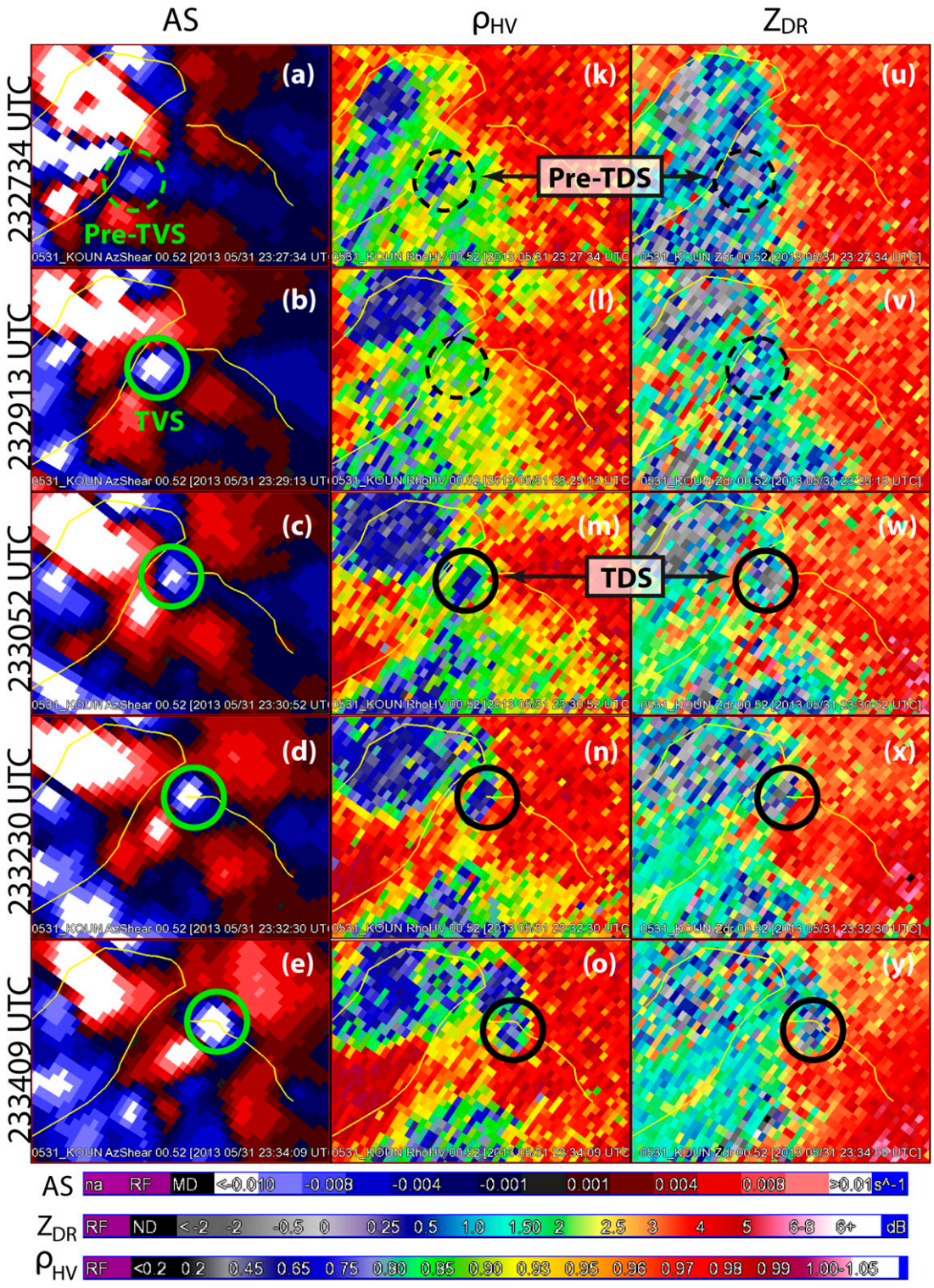

FIG. 6. KOUN observations of (a)–(j) AS (s^{-1}), (k)–(t) ρ_{hv} (unitless), and (u)–(dd) Z_{DR} (dB) at 0.5° from 2327 to 2343 UTC. The outlines of the El Reno tornado track and the anticyclonic tornado track are both drawn in yellow, as in Fig. 1. The AS minimum (TDS) associated with the anticyclonic tornado is circled in green (black); if dashed, the signature is considered pre- or posttornadic.

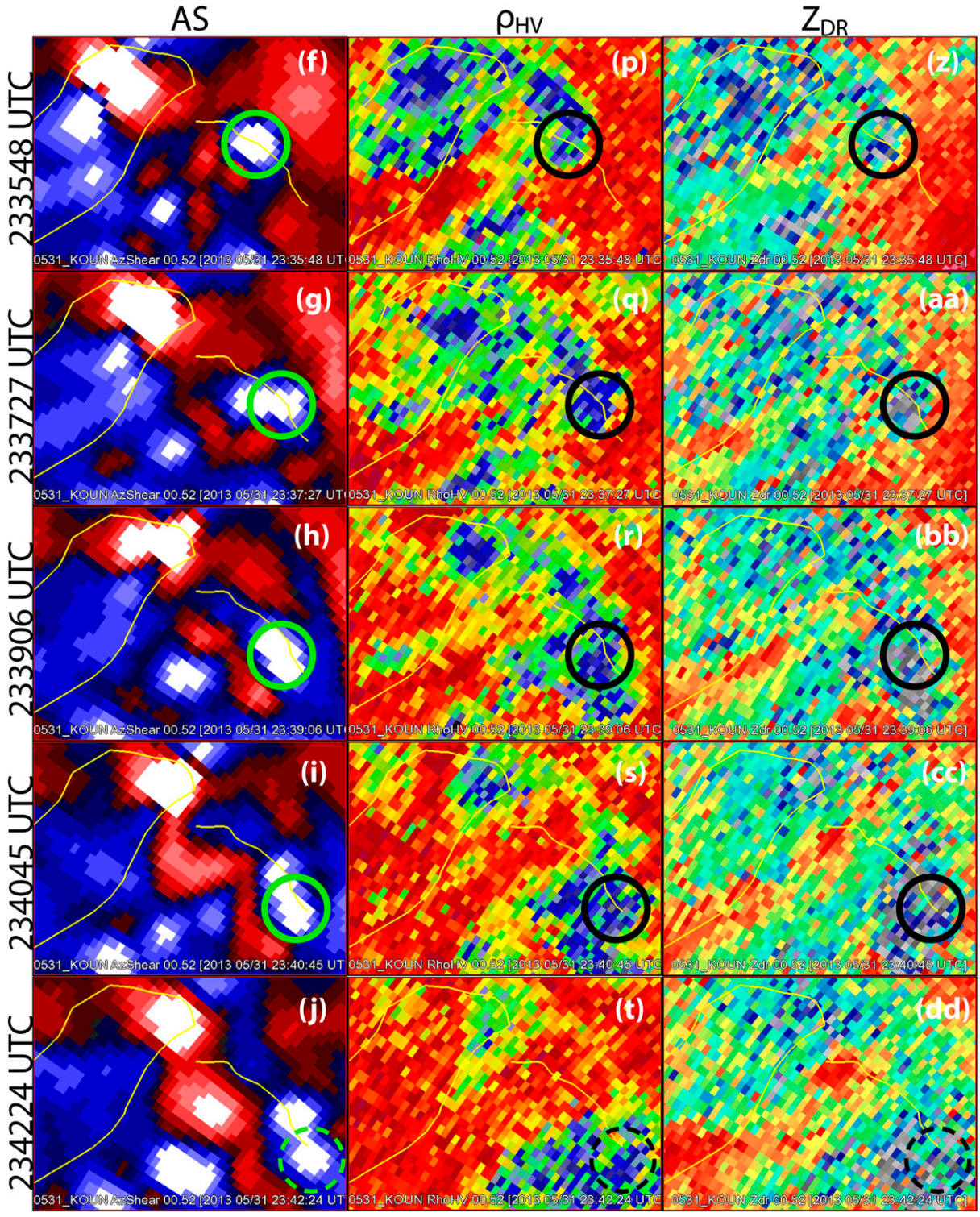

FIG. 6. (*Continued*)

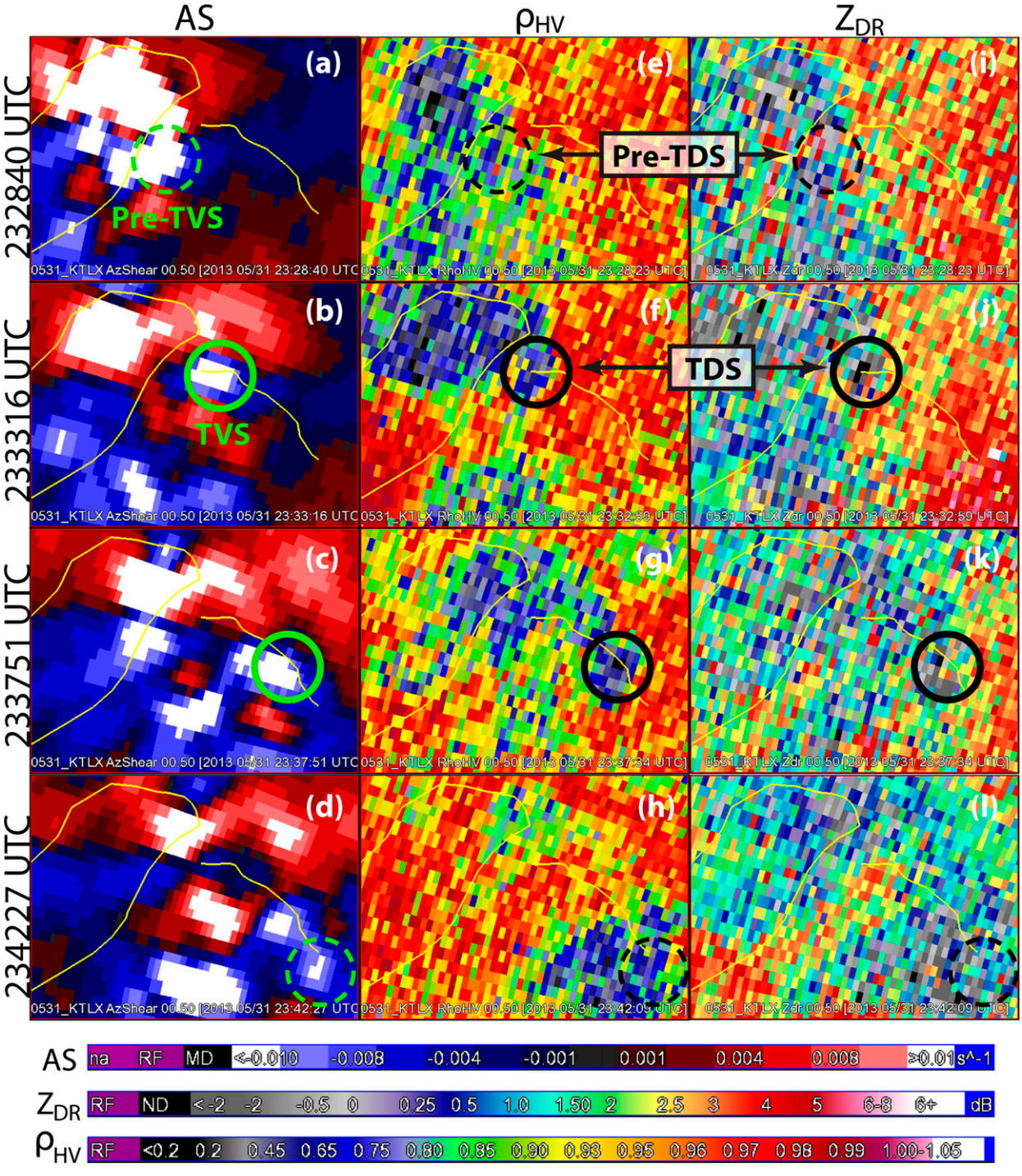

FIG. 7. As in Fig. 6, but for KTLX observations of (a)–(d) AS, (e)–(h) ρ_{hv}, and (i)–(l) Z_{DR}.

Although this smaller, dissipating storm was not associated with any severe weather, the rapid, polarimetric KOUN observations allowed for more complete documentation of its demise and afforded improved understanding of the low-Z_{DR} appendage's significance.

5. Conclusions

A dual-polarized WSR-88D (KOUN) collected rapid, sectorized volumes in a complex of severe thunderstorms in central Oklahoma on 31 May 2013. These

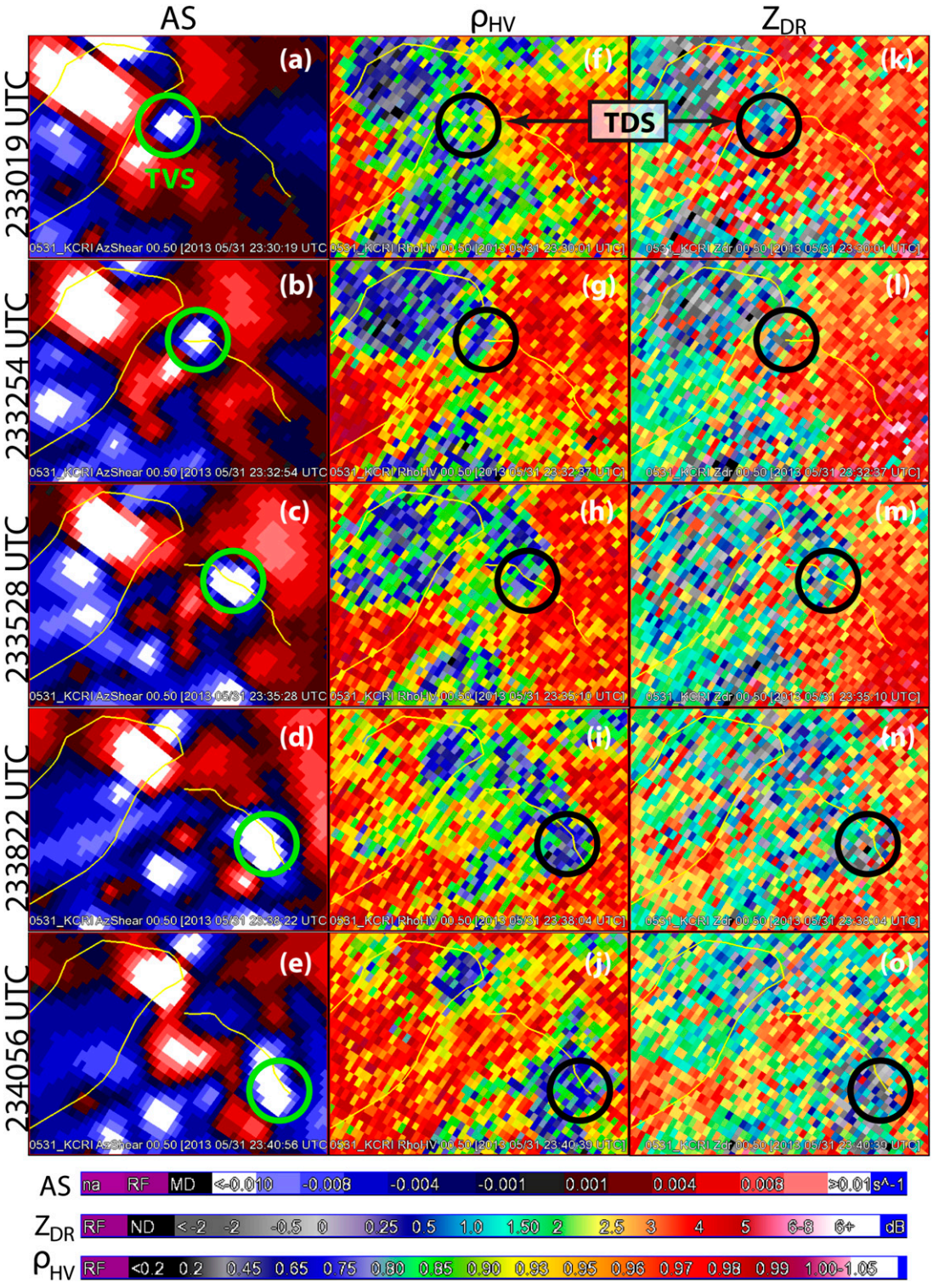

FIG. 8. As in Fig. 6, but for KCRI observations of (a)–(e) AS, (f)–(j) ρ_{hv}, and (k)–(o) Z_{DR}.

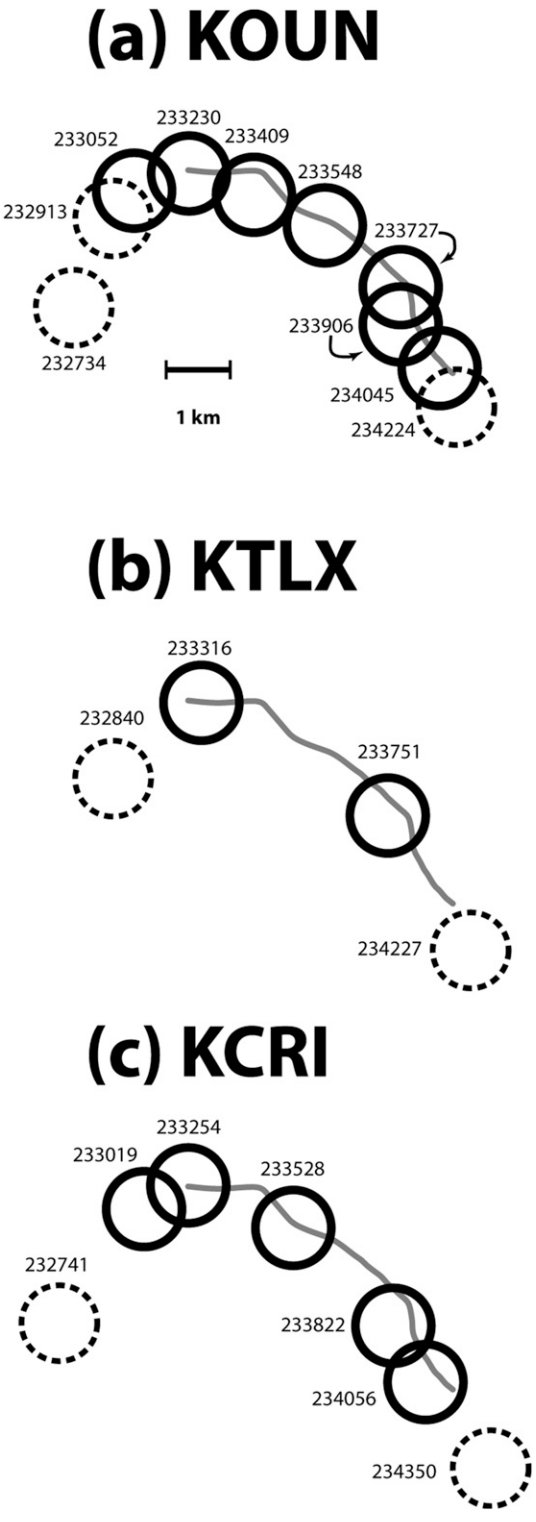

FIG. 9. Approximate track of the TDS center relative to the surveyed surface damage track of the anticyclonic tornado (Fig. 1). The use of open circles (which are all the same size) is intended to convey uncertainty in the exact location of the TDS center, not the size of the TDS itself. If the circle is dashed, the TDS is considered pre- or posttornadic. (Damage track courtesy of J. Snyder.)

observations enabled improved understanding of severe thunderstorm dynamics and microphysics when compared with contemporaneous observations collected by a nearby operational WSR-88D (KTLX, operating in AVSET mode with a 4.1-min volume update interval) and a nearly collocated experimental WSR-88D (KCRI, operating in SAILS mode with a 5.1-min volume update interval). In particular, KOUN provided faster and clearer polarimetric observations of 1) merging MLUs, 2) the descent of a volume of giant hail including a 160-mm hailstone (Witt 2014), 3) the rapid formation of a TDS in an anticyclonic tornado, and 4) hydrometeor size sorting in a dissipating cell.

We offer the following conclusions:

- As demonstrated by the KCRI observations used in this study, the SAILS VCP provides additional observations at low-elevation angles at the expense of less frequent observations at higher-elevation angles. While more frequent low-elevation observations are clearly advantageous to operational forecasters in rapidly evolving severe weather scenarios, they are detrimental to the detection and study of elevated features such as MLUs. Recent studies (e.g., Hastings et al. 2012, 2014; Marquis et al. 2012; Tanamachi et al. 2015) suggest that MLUs (and interactions between them and other dynamical storm features) may play a nontrivial role in the complex dynamics modulating tornadogenesis, maintenance, and decay.
- The KOUN rapid scanning of the severe storms on 31 May 2013 was enabled, at least in part, by the ability to collect user-specified sectors on demand. The KOUN operator was able to shift the radar sector to concentrate observations on areas of interest within the storm complex, rather than revisiting every beam position uniformly as in the operational VCPs. This practice resulted in more frequent observations of the entire storm volume and was clearly advantageous in the interpretation of MLU interactions and mergers.
- We showed an example in which the automated timing of an operational WSR-88D (KTLX) volume scan delayed detection of a developing tornado by 3 or 4 min (Figs. 7b,f,j), while a more rapidly scanned WSR-88D captured the TDS within a minute of tornadogenesis (Figs. 6m,w). More frequent operational radar volume updates would ensure that TDSs would be detected sooner after tornadogenesis. While KCRI's use of SAILS shortened the tornadic vortex signature (TVS)/TDS detection time considerably (Figs. 8a,f,k) and increased the frequency of tornado observations relative to KTLX, its total volume update time was still longer than that of either KTLX or KOUN. The motion of the tornado was better

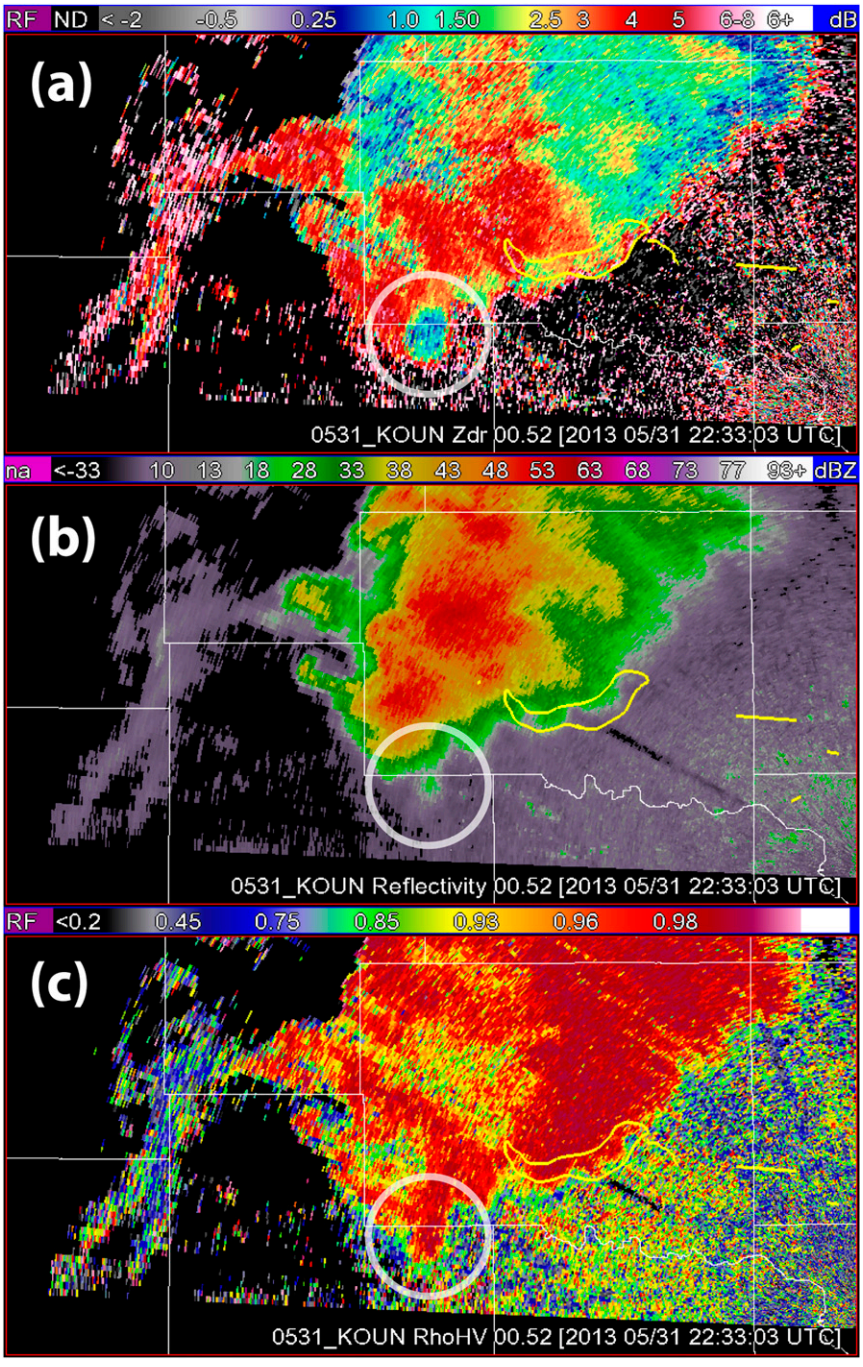

FIG. 10. KOUN observations of (a) Z_{DR} (dB), (b) Z (dBZ), and (c) ρ_{hv} (unitless) at 0.5° at 2233 UTC in the organizing El Reno storm complex. A low-Z_{DR} appendage is circled in white.

resolved with more frequent low-elevation scanning, showing changes in the tornado's direction and speed (Fig. 9). These details could inform precise placement and duration of tornado warning polygons. Earlier and more frequent TDS detection may enhance the wording and accuracy of follow-up products, such as severe weather statements. These detections may also strengthen a forecaster's ability to provide decision-making support to stakeholders such as emergency managers, large venue operators, and first responders.

- The use of more pulses per radial in the KOUN observations resulted in the calculation of more statistically robust moments and clearer fields overall compared to KTLX and KCRI. The midlevel Z_{DR}

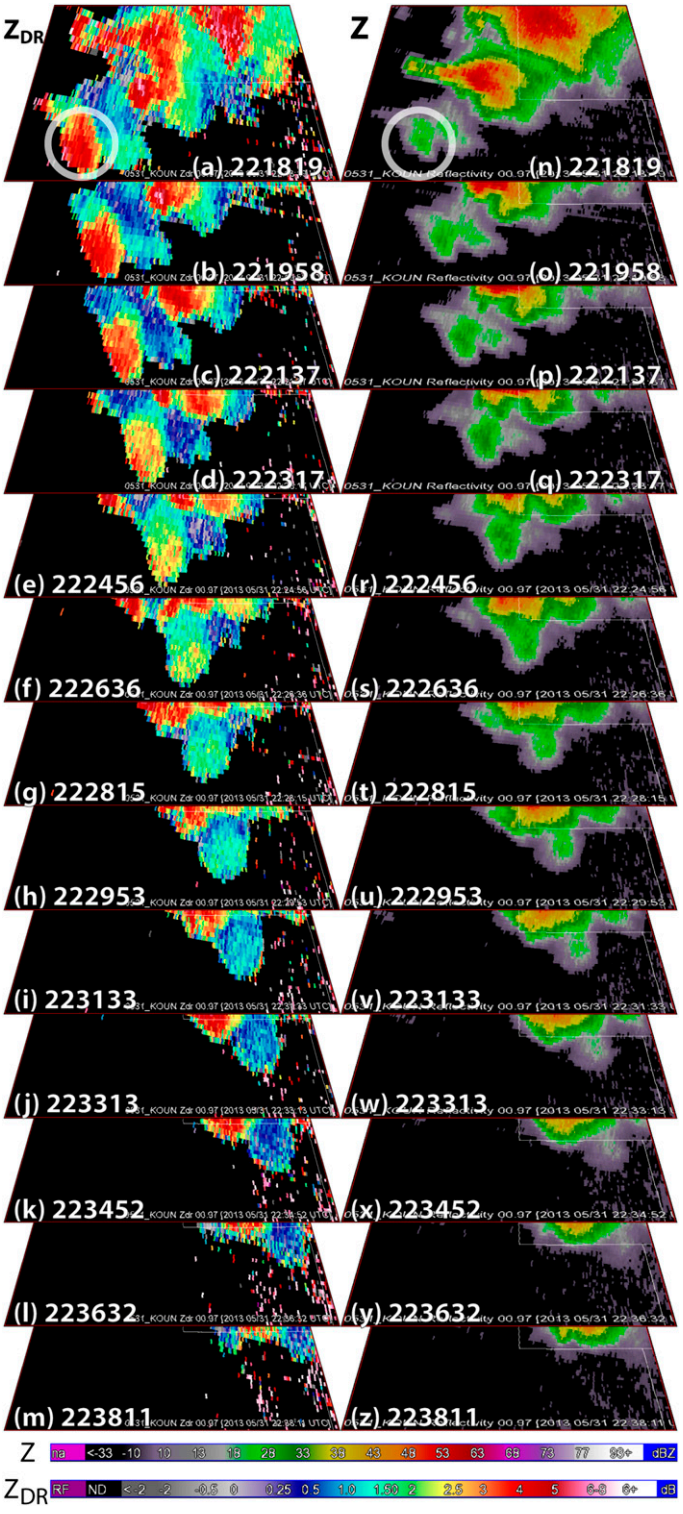

FIG. 11. KOUN observations of (a)–(m) Z_{DR} (dB) and (n)–(z) Z (dBZ) at 1.0° from 2218 to 2239 UTC in the collapsing cell southwest of the intensifying El Reno storm. The high-Z_{DR} appendage that turned into the low-Z_{DR} appendage in Fig. 10 is circled in white in (a) and (n).

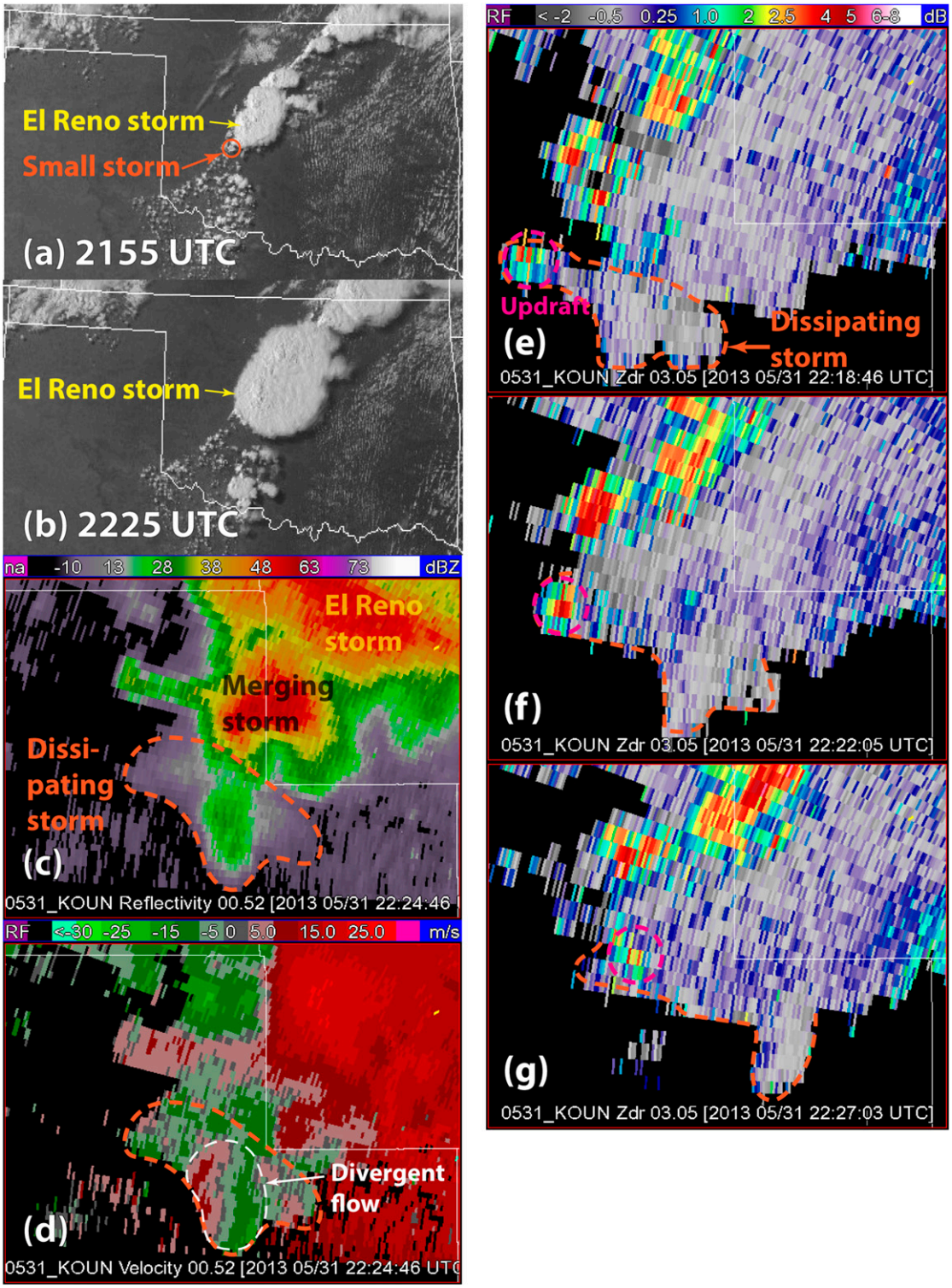

FIG. 12. Visible satellite image over Oklahoma taken at (a) 2155 and (b) 2225 UTC, showing the southward expansion of the El Reno storm's anvil over a smaller, developing storm that subsequently dissipated, forming the low-Z_{DR} appendage (Fig. 10). Satellite imagery courtesy of UCAR (http://www2.mmm.ucar.edu/imagearchive). KOUN observations at 0.5° of (c) Z and (d) Doppler velocity at 2224:46 UTC, showing the divergence (dashed white outline) associated with the remnants of the dissipating storm's precipitation core (dashed orange outline). KOUN observations at 3.0° of Z_{DR} at (e) 2218:46, (f) 2222:05, and (g) 2227:03 UTC. The final updraft pulse (Z_{DR} column) associated with this dissipating storm is circled in magenta.

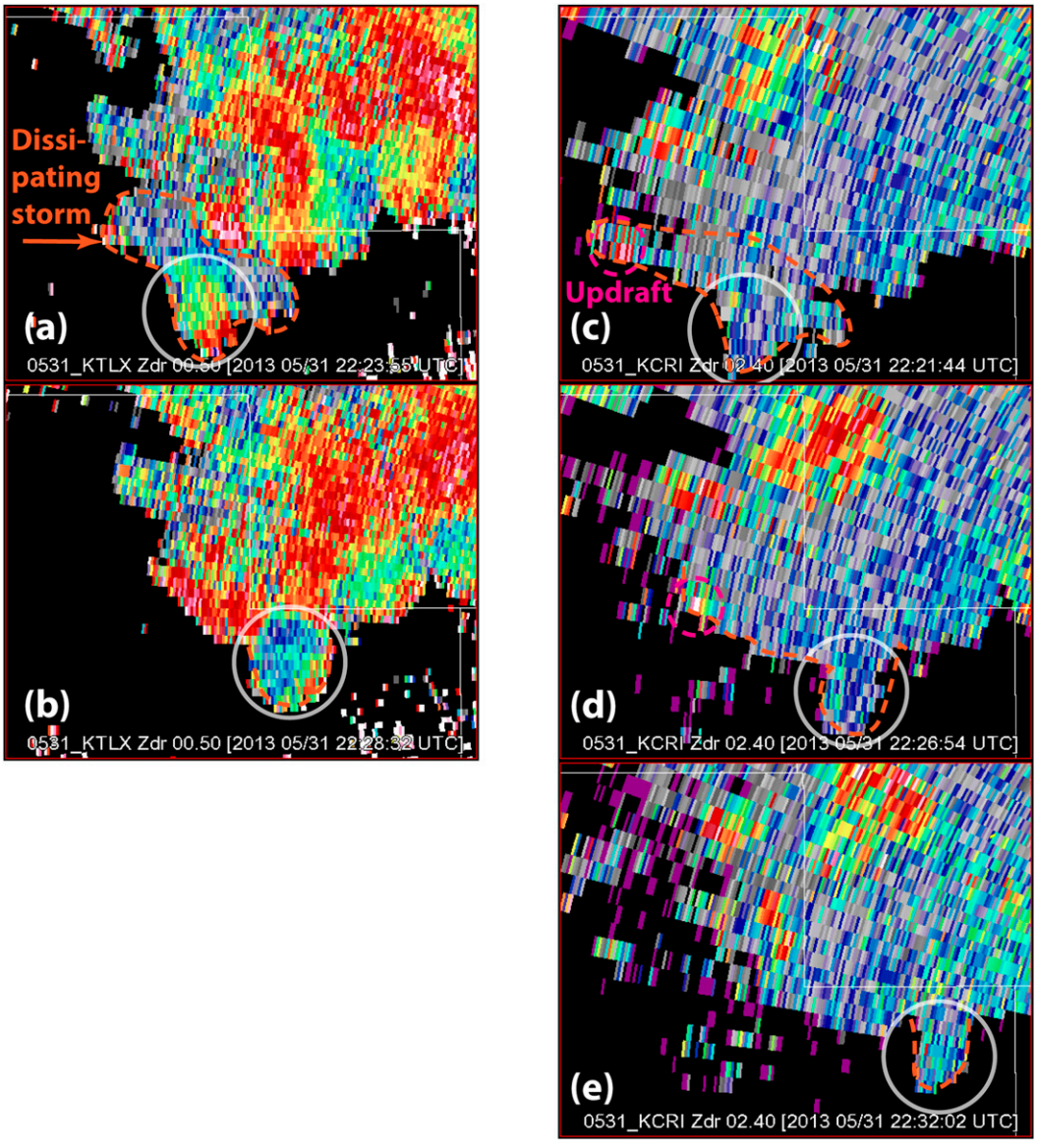

FIG. 13. KTLX Z_{DR} observations at 0.5° taken at (a) 2223:55 and (b) 2228:32 UTC, showing how the appendage (circled in white) associated with the dissipating storm (orange dashed outline) transitions from a relatively high-Z_{DR} feature to a low-Z_{DR} feature between the two consecutive scans. KCRI Z_{DR} observations at 2.4° of Z_{DR} taken at (c) 2221:44, (d) 2226:54, and (e) 2232:02 UTC. The final updraft pulse (Z_{DR} column) associated with this dissipating storm is circled in dashed magenta.

field in particular was clearer and easier to interpret. Small-scale features such as Z_{DR} columns and descending hail signatures were more easily distinguished in individual KOUN volumes than in the KTLX and KCRI volumes. We recommend that a future DP PAR be configured to collect more pulses in those radials where higher concentrations of scatterers are detected than in those where few or none are detected.

Although polarimetric WSR-88D observations have proven to be of enormous value in diagnosing and nowcasting convective storms, the examples provided in this study demonstrate that more rapid (~1 min) and robust (i.e., using a larger number of pulses than the conventional 32) polarimetric observations can serve to amplify those advantages for both operational and research meteorologists. As of this writing, a DP PAR demonstrator is undergoing testing at NSSL.

Acknowledgments. Funding for this research was provided by NOAA/Office of Oceanic and Atmospheric

Research under NOAA–University of Oklahoma Cooperative Agreement NA11OAR4320072, U.S. Department of Commerce. We thank Valery Melinkov and Joe Chrisman for their assistance with data collection, and Eddie Forren and Richard Adams for processing the KOUN observations. KTLX and KCRI observations were obtained from the National Climatic Data Center. The El Reno tornado damage track was provided by the National Weather Service. Jeff Snyder provided the anticyclonic tornado's damage track. We appreciate the insights of Rick Smith, Todd Lindley, and Arthur Witt. Vivek Mahale, Charles Kuster, and three additional anonymous individuals kindly reviewed this manuscript.

REFERENCES

Agee, E. M., J. T. Snow, and P. R. Clare, 1976: Multiple vortex features in the tornado cyclone and the occurrence of tornado families. *Mon. Wea. Rev.*, **104**, 552–563, doi:10.1175/1520-0493(1976)104<0552:MVFITT>2.0.CO;2.

Aydin, K., T. A. Seliga, and V. Balaji, 1986: Remote sensing of hail with a dual linear polarization radar. *J. Climate Appl. Meteor.*, **25**, 1475–1484, doi:10.1175/1520-0450(1986)025<1475:RSOHWA>2.0.CO;2.

Balakrishnan, N., and D. S. Zrnic, 1990: Use of polarization to characterize precipitation and discriminate large hail. *J. Atmos. Sci.*, **47**, 1525–1540, doi:10.1175/1520-0469(1990)047<1525:UOPTCP>2.0.CO;2.

Bluestein, H. B., M. M. French, R. L. Tanamachi, S. Frasier, K. Hardwick, F. Junyent, and A. L. Pazmany, 2007: Close-range observations of tornadoes in supercells made with a dual-polarization, X-band, mobile Doppler radar. *Mon. Wea. Rev.*, **135**, 1522–1543, doi:10.1175/MWR3349.1.

——, ——, I. PopStefanija, R. T. Bluth, and J. B. Knorr, 2010: A mobile, phased-array Doppler radar for the study of severe convective storms. *Bull. Amer. Meteor. Soc.*, **91**, 579–600, doi:10.1175/2009BAMS2914.1.

——, and Coauthors, 2014: Radar in atmospheric sciences and related research: Current systems, emerging technology, and future needs. *Bull. Amer. Meteor. Soc.*, **95**, 1850–1861, doi:10.1175/BAMS-D-13-00079.1.

——, J. C. Snyder, and J. B. Houser, 2015: A multiscale overview of the El Reno, Oklahoma, tornadic supercell of 31 May 2013. *Wea. Forecasting*, **30**, 525–552, doi:10.1175/WAF-D-14-00152.1.

Bodine, D. J., R. D. Palmer, and G. Zhang, 2014: Dual-wavelength polarimetric radar analyses of tornadic debris signatures. *J. Appl. Meteor. Climatol.*, **53**, 242–261, doi:10.1175/JAMC-D-13-0189.1.

Bowden, K. A., P. L. Heinselman, D. M. Kingfield, and R. P. Thomas, 2015: Impacts of phased-array radar data on forecaster performance during severe hail and wind events. *Wea. Forecasting*, **30**, 389–404, doi:10.1175/WAF-D-14-00101.1.

Bringi, V. N., T. A. Seliga, and S. M. Cherry, 1984: Hail detection with a differential reflectivity radar. *Science*, **225**, 1145–1147, doi:10.1126/science.225.4667.1145.

Brown, R. A., and V. T. Wood, 2012: Simulated vortex detection using a four-face phased-array Doppler radar. *Wea. Forecasting*, **27**, 1598–1603, doi:10.1175/WAF-D-12-00059.1.

——, ——, and D. Sirmans, 2002: Improved tornado detection using simulated and actual WSR-88D data with enhanced resolution. *J. Atmos. Oceanic Technol.*, **19**, 1759–1771, doi:10.1175/1520-0426(2002)019<1759:ITDUSA>2.0.CO;2.

——, B. A. Flickinger, E. Forren, D. M. Schultz, D. Sirmans, P. L. Spencer, V. T. Wood, and C. L. Ziegler, 2005a: Improved detection of severe storms using experimental fine-resolution WSR-88D measurements. *Wea. Forecasting*, **20**, 3–14, doi:10.1175/WAF832.1.

——, V. T. Wood, R. M. Steadham, R. R. Lee, B. A. Flickinger, and D. Sirmans, 2005b: New WSR-88D volume coverage pattern 12: Results of field tests. *Wea. Forecasting*, **20**, 385–393, doi:10.1175/WAF848.1.

Burgess, D., V. Melnikov, D. Priegnitz, R. A. Brown, P. L. Heinselman, E. R. Mansell, and V. T. Wood, 2014: Tornadic supercells in central Oklahoma on May 19, 20, and 31 of 2013: NSSL radar data. *Proc. Special Symp. on Severe Local Storms: The Current State of the Science and Understanding Impacts*, Atlanta, GA, Amer. Meteor. Soc., 825. [Available online at https://ams.confex.com/ams/94Annual/webprogram/Paper233974.html.]

Chrisman, J. N., 2009: Automated Volume Scan Evaluation and Termination (AVSET)—A simple technique to achieve faster volume scan updates. Preprints, *34th Conf. on Radar Meteorology*, Williamsburg, VA, Amer. Meteor. Soc., P4.4. [Available online at https://ams.confex.com/ams/pdfpapers/155324.pdf.]

——, 2014: The continuing evolution of dynamic scanning. *NEXRAD Now*, No. 23, NOAA/NWS/Radar Operations Center, Norman, OK, 8–13.

Crowe, C. C., W. A. Petersen, L. D. Carey, and D. J. Cecil, 2010: A dual-polarization investigation of tornado-warned cells associated with Hurricane Rita. *Electron. J. Oper. Meteor.*, **11** (4). [Available online at http://www.nwas.org/ej/2010-EJ4/.]

——, C. J. Schultz, M. R. Kumjian, L. D. Carey, and W. A. Petersen, 2012: Use of dual-polarization signatures in diagnosing tornadic potential. *Electron. J. Oper. Meteor.*, **13**, 57–78. [Available online at http://www.nwas.org/ej/pdf/2012-EJ5.pdf.]

Dawson, D. T., E. R. Mansell, Y. Jung, L. J. Wicker, M. R. Kumjian, and M. Xue, 2014: Low-level Z_{DR} signatures in supercell forward flanks: The role of size sorting and melting of hail. *J. Atmos. Sci.*, **71**, 276–299, doi:10.1175/JAS-D-13-0118.1.

——, ——, and M. R. Kumjian, 2015: Does wind shear cause hydrometeor size sorting? *J. Atmos. Sci.*, **72**, 340–348, doi:10.1175/JAS-D-14-0084.1.

Doviak, R. J., and D. S. Zrnić, 1993: *Doppler Weather Radar and Observations.* 2nd ed. Academic Press, 562 pp.

Edwards, R., 2014: Characteristics of supercellular satellite tornadoes. *Proc. 27th Conf. on Severe Local Storms*, Madison, WI, Amer. Meteor. Soc., 17.5. [Available online at https://ams.confex.com/ams/27SLS/webprogram/Paper254326.html.]

Federal Coordinator for Meteorological Services and Supporting Research, 2013: Part A: System concepts, responsibilities, and procedures. Doppler Radar Meteorological Observations, Federal Meteorological Handbook 11, U.S. Department of Commerce Doc. FCM-H11A-2013, 49 pp. [Available online at http://www.ofcm.gov/fmh11/fmh11parta/pdf/FMH-11%20Pt%20A%20Feb%202013%20All.pdf.]

Frame, J., and P. Markowski, 2013: Dynamical influences of anvil shading on simulated supercell thunderstorms. *Mon. Wea. Rev.*, **141**, 2802–2820, doi:10.1175/MWR-D-12-00146.1.

French, M. M., H. B. Bluestein, I. PopStefanija, C. A. Baldi, and R. T. Bluth, 2013: Reexamining the vertical development of tornadic vortex signatures in supercells. *Mon. Wea. Rev.*, **141**, 4576–4601, doi:10.1175/MWR-D-12-00315.1.

——, D. W. Burgess, E. R. Mansell, and L. J. Wicker, 2014a: Bulk hook echo raindrop sizes retrieved using mobile, polarimetric

Doppler radar observations. *J. Climate Appl. Meteor.*, **54**, 423–450, doi:10.1175/JAMC-D-14-0171.1.

——, H. B. Bluestein, I. PopStefanija, C. A. Baldi, and R. T. Bluth, 2014b: Mobile, phased-array, Doppler radar observations of tornadoes at X band. *Mon. Wea. Rev.*, **142**, 1010–1036, doi:10.1175/MWR-D-13-00101.1.

Friedrich, K., E. A. Kalina, F. J. Masters, and C. R. Lopez, 2013: Drop-size distributions in thunderstorms measured by optical disdrometers during VORTEX2. *Mon. Wea. Rev.*, **141**, 1182–1203, doi:10.1175/MWR-D-12-00116.1.

Hastings, R. M., Y. P. Richardson, and P. M. Markowski, 2012: Mergers in supercell environments. Part II: Tornadogenesis potential during merger as evaluated by changes in the near-surface low-level mesocyclone. *Proc. 26th Conf. on Severe Local Storms*, Nashville, TN, Amer. Meteor. Soc., 143. [Available online at https://ams.confex.com/ams/26SLS/webprogram/Paper212524.html.]

——, ——, and ——, 2014: Simulation of near-surface mesocyclogenesis during mergers between mature and nascent supercells. *Proc. 27th Conf. on Severe Local Storms*, Madison, WI, Amer. Meteor. Soc., 3B.2. [Available online at https://ams.confex.com/ams/27SLS/webprogram/Paper255837.html.]

Heinselman, P. L., and A. V. Ryzhkov, 2006: Validation of polarimetric hail detection. *Wea. Forecasting*, **21**, 839–850, doi:10.1175/WAF956.1.

——, and S. M. Torres, 2011: High-temporal-resolution capabilities of the National Weather Radar Testbed phased-array radar. *J. Climate Appl. Meteor.*, **50**, 579–593, doi:10.1175/2010JAMC2588.1.

——, D. L. Priegnitz, K. L. Manross, T. M. Smith, and R. W. Adams, 2008: Rapid sampling of severe storms by the National Weather Radar Testbed Phased Array Radar. *Wea. Forecasting*, **23**, 808–824, doi:10.1175/2008WAF2007071.1.

——, D. S. LaDue, and H. Lazrus, 2012: Exploring impacts of rapid-scan radar data on NWS warning decisions. *Wea. Forecasting*, **27**, 1031–1044, doi:10.1175/WAF-D-11-00145.1.

——, ——, D. M. Kingfield, and R. Hoffman, 2015: Tornado warning decisions using phased-array radar data. *Wea. Forecasting*, **30**, 57–78, doi:10.1175/WAF-D-14-00042.1.

Houser, J. B., H. B. Bluestein, and J. C. Snyder, 2015: Rapid-scan, polarimetric, Doppler-radar observations of tornadogenesis and tornado dissipation in a tornadic supercell: The ''El Reno, Oklahoma'' storm of 24 May 2011. *Mon. Wea. Rev.*, **143**, 2685–2710, doi:10.1175/MWR-D-14-00253.1.

Illingworth, A. J., J. W. F. Goddard, and S. M. Cherry, 1987: Polarization radar studies of precipitation development in convective storms. *Quart. J. Roy. Meteor. Soc.*, **113**, 469–489, doi:10.1002/qj.49711347604.

Istok, M. J., and Coauthors, 2009: WSR-88D dual polarization initial operational capabilities. *25th Conf. on Int. Interactive Information and Processing Systems (IIPS) for Meteorology, Oceanography, and Hydrology*, Phoenix, AZ, Amer. Meteor. Soc., 15.5. [Available online at https://ams.confex.com/ams/pdfpapers/148927.pdf.]

Jung, Y., M. Xue, and G. Zhang, 2010: Simulations of polarimetric radar signatures of a supercell storm using a two-moment bulk microphysics scheme. *J. Climate Appl. Meteor.*, **49**, 146–163, doi:10.1175/2009JAMC2178.1.

Kosiba, K., J. Wurman, Y. Richardson, P. Markowski, P. Robinson, and J. Marquis, 2013: Genesis of the Goshen County, Wyoming, tornado on 5 June 2009 during VORTEX2. *Mon. Wea. Rev.*, **141**, 1157–1181, doi:10.1175/MWR-D-12-00056.1.

Kumjian, M. R., 2013: Principles and applications of dual-polarization weather radar. Part II: Warm- and cold-season applications. *J. Oper. Meteor.*, **1**, 243–264, doi:10.15191/nwajom.2013.0120.

——, and A. V. Ryzhkov, 2008: Polarimetric signatures in supercell thunderstorms. *J. Appl. Meteor. Climatol.*, **47**, 1940–1961, doi:10.1175/2007JAMC1874.1.

——, and A. D. Schenkman, 2008: Interpretation of the ''flying eagle'' radar signature in supercells. Preprints, *24th Conf. on Severe Local Storms*, Savannah, GA, Amer. Meteor. Soc., P14.2. [Available online at https://ams.confex.com/ams/pdfpapers/141917.pdf.]

——, and A. V. Ryzhkov, 2009: Storm-relative helicity revealed from polarimetric radar measurements. *J. Atmos. Sci.*, **66**, 667–685, doi:10.1175/2008JAS2815.1.

——, and ——, 2012: The impact of size sorting on the polarimetric radar variables. *J. Atmos. Sci.*, **69**, 2042–2060, doi:10.1175/JAS-D-11-0125.1.

——, ——, V. M. Melnikov, and T. J. Schuur, 2010: Rapid-scan super-resolution observations of a cyclic supercell with a dual-polarization WSR-88D. *Mon. Wea. Rev.*, **138**, 3762–3786, doi:10.1175/2010MWR3322.1.

——, A. P. Khain, N. Benmoshe, E. Ilotoviz, A. V. Ryzhkov, and V. T. J. Phillips, 2014: The anatomy and physics of Z_{DR} columns: Investigating a polarimetric radar signature with a spectral bin microphysical model. *J. Appl. Meteor. Climatol.*, **53**, 1820–1843, doi:10.1175/JAMC-D-13-0354.1.

Kurdzo, J. M., D. J. Bodine, B. L. Cheong, and R. D. Palmer, 2015a: High-temporal resolution polarimetric X-band Doppler radar observations of the 20 May 2013 Moore, Oklahoma, tornado. *Mon. Wea. Rev.*, **143**, 2711–2735, doi:10.1175/MWR-D-14-00357.1.

——, F. Nai, D. J. Bodine, R. D. Palmer, J. J. Lujan, A. Mahre, and A. Byrd, 2015b: Observations of severe local storms and tornadoes with the Atmospheric Imaging Radar. *Proc. 37th Conf. on Radar Meteorology*, Norman, OK, Amer. Meteor. Soc., 6B.1. [https://ams.confex.com/ams/37RADAR/webprogram/Paper275524.html.]

Kuster, C. M., P. Burke, and A. A. Taylor, 2012: An 11-year radar-based study of tornadic thunderstorms over central Oklahoma. *Electron. J. Severe Storms Meteor.*, **7** (8). [Available online at http://www.ejssm.org/ojs/index.php/ejssm/issue/view/41.]

——, P. L. Heinselman, and M. Austin, 2015a: 31 May 2013 El Reno tornadoes: Advantages of rapid-scan phased-array radar data from a warning forecaster's perspective. *Wea. Forecasting*, **30**, 933–956, doi:10.1175/WAF-D-14-00142.1.

——, ——, and T. Schuur, 2015b: Rapid sampling of radar precursor signatures associated with downbursts in central Oklahoma on 14 June 2011. *Proc. 30th Conf. on Environmental Information Processing Technologies*, Atlanta, GA, Amer. Meteor. Soc., 6.3. [Available online at https://ams.confex.com/ams/94Annual/webprogram/Paper233824.html.]

LaDue, D. S., P. L. Heinselman, and J. F. Newman, 2010: Strengths and limitations of current radar systems for two stakeholder groups in the southern plains. *Bull. Amer. Meteor. Soc.*, **91**, 899–910, doi:10.1175/2009BAMS2830.1.

Lakshmanan, V., T. Smith, G. Stumpf, and K. Hondl, 2007: The Warning Decision Support System–Integrated Information. *Wea. Forecasting*, **22**, 596–612, doi:10.1175/WAF1009.1.

Loney, M. L., D. S. Zrnić, J. M. Straka, and A. V. Ryzhkov, 2002: Enhanced polarimetric radar signatures above the melting level in a supercell storm. *J. Appl. Meteor.*, **41**, 1179–1194, doi:10.1175/1520-0450(2002)041<1179:EPRSAT>2.0.CO;2.

Maki, M., and Coauthors, 2008: X-band polarimetric radar network in the Tokyo metropolitan area—X-NET. *Proc. Fifth European Conf. on Radar Meteorology and Hydrology*, Helsinki, Finland, Finnish Meteorological Institute, 5 pp.

Marquis, J., Y. Richardson, P. Markowski, D. Dowell, and J. Wurman, 2012: Tornado maintenance investigated with high-resolution dual-Doppler and EnKF analysis. *Mon. Wea. Rev.*, **140**, 3–27, doi:10.1175/MWR-D-11-00025.1.

McDonald, J. R., and K. C. Mehta, 2006: A recommendation for an enhanced Fujita scale (EF-scale). Texas Tech University, Lubbock, TX, 111 pp. [Available online at http://www.depts.ttu.edu/nwi/Pubs/FScale/EFScale.pdf.]

McLaughlin, D., and Coauthors, 2009: Short-wavelength technology and the potential for distributed networks of small radar systems. *Bull. Amer. Meteor. Soc.*, **90**, 1797–1817, doi:10.1175/2009BAMS2507.1.

Melnikov, V. M., D. Zrnic, D. W. Burgess, and E. R. Mansell, 2014: Observations of hail cores of tornadic thunderstorms with three polarimetric radars. *30th Conf. on Environmental Information Processing Technologies*, Atlanta, GA, Amer. Meteor. Soc., 11. [Available online at https://ams.confex.com/ams/94Annual/webprogram/Paper233038.html.]

National Climatic Data Center, cited 2015: Storm events database. Accessed 3 February 2015. [Available online at http://www.ncdc.noaa.gov/stormevents.]

National Research Council, 2002: *Weather Radar Technology beyond NEXRAD.* The National Academies Press, 96 pp.

National Weather Service, 2014a: Service assessment: May 2013 Oklahoma tornadoes and flash flooding. Silver Spring, MD, 63 pp. [Available online at http://www.nws.noaa.gov/os/assessments/pdfs/13oklahoma_tornadoes.pdf.]

——, cited 2014b: The May 31–June 1, 2013 tornado and flash flooding event. National Weather Service Forecast Office, Norman, OK. [Available online at http://www.srh.noaa.gov/oun/?n=events-20130531.]

Orzeł, K. A., and Coauthors, 2011: Mobile X-band dual polarization phased-array radar: System requirements and development. *Proc. 35th Conf. on Radar Meteorology*, Pittsburgh, PA, Amer. Meteor. Soc., 14A.4. [Available online at https://ams.confex.com/ams/35Radar/webprogram/Paper191899.html.]

Palmer, R. D., and Coauthors, 2011: Observations of the 10 May 2010 tornado outbreak using OU-PRIME: Potential for new science with high-resolution polarimetric radar. *Bull. Amer. Meteor. Soc.*, **92**, 871–891, doi:10.1175/2011BAMS3125.1.

Pazmany, A. L., J. B. Mead, H. B. Bluestein, J. C. Snyder, and J. B. Houser, 2013: A mobile, rapid-scanning, X-band, polarimetric, (RaXPol) Doppler-radar system. *J. Atmos. Oceanic Technol.*, **30**, 1398–1413, doi:10.1175/JTECH-D-12-00166.1.

Picca, J., and A. V. Ryzhkov, 2012: A dual-wavelength polarimetric analysis of the 16 May 2010 Oklahoma City extreme hailstorm. *Mon. Wea. Rev.*, **140**, 1385–1403, doi:10.1175/MWR-D-11-00112.1.

Priegnitz, D. L., S. M. Torres, and P. L. Heinselman, 2013: Enhancements to the National Weather Radar Testbed phased array radar storm tracking function. *Proc. 29th Conf. on Environmental Information Processing Technologies*, Austin, TX, Amer. Meteor. Soc., 19. [Available online at https://ams.confex.com/ams/93Annual/webprogram/Paper217344.html.]

Romine, G. S., D. W. Burgess, and R. B. Wilhelmson, 2008: A dual-polarization-radar-based assessment of the 8 May 2003 Oklahoma City area tornadic supercell. *Mon. Wea. Rev.*, **136**, 2849–2870, doi:10.1175/2008MWR2330.1.

Ryzhkov, A. V., T. J. Schuur, D. W. Burgess, P. L. Heinselman, S. E. Giangrande, and D. S. Zrnic, 2005a: The Joint Polarization Experiment: Polarimetric rainfall measurements and hydrometeor classification. *Bull. Amer. Meteor. Soc.*, **86**, 809–824, doi:10.1175/BAMS-86-6-809.

——, ——, ——, and D. S. Zrnic, 2005b: Polarimetric tornado detection. *J. Appl. Meteor.*, **44**, 557–570, doi:10.1175/JAM2235.1.

Scharfenberg, K. A., and Coauthors, 2005: The Joint Polarization Experiment: Polarimetric radar in forecasting and warning decision making. *Wea. Forecasting*, **20**, 775–788, doi:10.1175/WAF881.1.

Schultz, C. J., and Coauthors, 2012: Dual-polarization tornadic debris signatures, Part I: Examples and utility in an operational setting. *Electron. J. Oper. Meteor.*, **13** (9), 120–137. [Available online at http://www.nwas.org/ej/pdf/2012-EJ9.pdf.]

Smith, T. M., and K. L. Elmore, 2004: The use of radial velocity derivatives to diagnose rotation and divergence. Preprints, *11th Conf. on Aviation, Range, and Aerospace*, Hyannis, MA, Amer. Meteor. Soc., P5.6. [Available online at https://ams.confex.com/ams/pdfpapers/81827.pdf.]

Snyder, J. C., and H. B. Bluestein, 2014: Some considerations for the use of high-resolution mobile radar data in tornado intensity determination. *Wea. Forecasting*, **29**, 799–827, doi:10.1175/WAF-D-14-00026.1.

——, ——, V. Venkatesh, and S. J. Frasier, 2013: Observations of polarimetric signatures in supercells by an X-band mobile Doppler radar. *Mon. Wea. Rev.*, **141**, 3–29, doi:10.1175/MWR-D-12-00068.1.

——, A. V. Ryzhkov, M. R. Kumjian, and J. Picca, 2015: A Z_{DR} column detection algorithm to examine convective storm updrafts. *Wea. Forecasting*, doi:10.1175/WAF-D-15-0068.1, in press.

Tanamachi, R. L., H. B. Bluestein, J. B. Houser, K. M. Hardwick, and S. J. Frasier, 2012: Mobile, X-band, polarimetric Doppler radar observations of the 4 May 2007 Greensburg, Kansas, tornadic supercell. *Mon. Wea. Rev.*, **140**, 2103–2125, doi:10.1175/MWR-D-11-00142.1.

——, P. L. Heinselman, and L. J. Wicker, 2015: Impacts of a storm merger on the 24 May 2011 El Reno, Oklahoma, tornadic supercell. *Wea. Forecasting*, **30**, 501–524, doi:10.1175/WAF-D-14-00164.1.

Van Den Broeke, M. S., J. M. Straka, and E. N. Rasmussen, 2008: Polarimetric radar observations at low levels during tornado life cycles in a small sample of classic southern plains supercells. *J. Appl. Meteor. Climatol.*, **47**, 1232–1247, doi:10.1175/2007JAMC1714.1.

Willingham, K. M., E. J. Thompson, K. W. Howard, and C. L. Dempsey, 2011: Characteristics of Sonoran Desert microbursts. *Wea. Forecasting*, **26**, 94–108, doi:10.1175/2010WAF2222388.1.

Witt, A., 2014: High-resolution phased array radar observations of an Oklahoma hailstorm producing extremely-large hail. *Proc. 27th Conf. on Severe Local Storms*, Madison, WI, Amer. Meteor. Soc., 165. [Available online at https://ams.confex.com/ams/27SLS/webprogram/Paper253994.html.]

Wurman, J., Y. Richardson, C. Alexander, S. Weygandt, and P. F. Zhang, 2007: Dual-Doppler and single-Doppler analysis of a tornadic storm undergoing mergers and repeated tornadogenesis. *Mon. Wea. Rev.*, **135**, 736–758, doi:10.1175/MWR3276.1.

——, P. Robinson, W.-C. Lee, C. R. Alexander, and K. A. Kosiba, 2008: Rapid-scan mobile radar 3D GBVTD and traditional analysis of tornadogenesis. Preprints, *24th Conf. on Severe Local Storms*, Savannah, GA, Amer. Meteor. Soc., P13.6. [Available online at https://ams.confex.com/ams/pdfpapers/142176.pdf.]

——, K. Kosiba, and P. Robinson, 2012: In situ, Doppler radar, and video observations of the interior structure of a tornado and wind–damage relationship. *Bull. Amer. Meteor. Soc.*, **94**, 835–846, doi:10.1175/BAMS-D-12-00114.1

——, ——, ——, and T. Marshall, 2014: The role of multiple vortex tornado structure in causing storm researcher fatalities. *Bull. Amer. Meteor. Soc.*, **95**, 31–45, doi:10.1175/BAMS-D-13-00221.1.

Zhang, G., R. J. Doviak, D. S. Zrnić, R. Palmer, L. Lei, and Y. Al-Rashid, 2011: Polarimetric phased-array radar for weather measurement: A planar or cylindrical configuration? *J. Atmos. Oceanic Technol.*, **28**, 63–73, doi:10.1175/2010JTECHA1470.1.

Zrnić, D. S., and Coauthors, 2007: Agile-beam phased array radar for weather observations. *Bull. Amer. Meteor. Soc.*, **88**, 1753–1766, doi:10.1175/BAMS-88-11-1753.

——, V. M. Melnikov, and R. J. Doviak, 2012: Issues and challenges for polarimetric measurement of weather with an agile beam phased array radar. NOAA/NSSL Rep., Norman, OK, 117 pp. [Available online at http://www.nssl.noaa.gov/publications/mpar_reports/MPAR-WEB_RPT-1_071412-7_May_2_2013_wo_comments.pdf.]